Miocene Subsidence and Surface Uplift of Southernmost Tibet Induced by Indian Subduction Dynamics

T. Shen, Gang Wang, Anne Replumaz, L. Husson, A. Webb, M. Bernet, Philippe Hervé Leloup, P. Zhang, Gweltaz Mahéo, K. Zhang

Miocene subsidence and surface uplift of southernmost Tibet induced by Indian subduction dynamics

T. Shen[1], G. Wang[1], A. Replumaz[2], L. Husson[2], A.A.G. Webb[3], M. Bernet[2], P.H. Leloup[4], P. Zhang[1], G. Mahéo[4], and K. Zhang[5]

[1]School of Earth Sciences, Center for Global Tectonics, and State Key Laboratory of Geological Processes and Mineral Resources, China University of Geosciences, Wuhan 430074, China

[2]Institut des Sciences de la Terre, Université Grenoble Alpes, CNRS, Grenoble 38000, France

[3] Division of Earth and Planetary Science and Laboratory for Space Research, University of Hong Kong, Hong Kong, China

[4]Laboratoire de Géologie de Lyon, CNRS UMR 5570, Université de Lyon 1, Villeurbanne 69622, France

[5] School of Earth Sciences and State Key Laboratory of Biogeology and Environmental Geology, China University of Geosciences, Wuhan 430074, China

Corresponding author: Tianyi Shen (shenty@cug.edu.cn)

Key Points:

- Gangdese batholith experienced reheating between ~28 and 20 Ma, followed by rapid cooling between 20-17 Ma at a rate of ~50 °C/Myr
- The northward migration of the Indian continent created a wave of dynamic topography that caused the successive subsidence and uplift
- The Kailas basin is a unique occurrence of a perched basin that owes its existence to dynamic deflection within a mountain belt

Abstract

The Indus-Yarlung suture of southernmost Tibet marks the initial collisional zone, the ongoing India-Asia collision, and yet more than ~30 million years after the onset of collision, a thick detrital sedimentary unit was deposited just north of the suture: the Kailas Formation. The mechanism permitting subsidence of the deep intracontinental Kailas basin in a compressional tectonic regime remains uncertain. We present new apatite (16-11 Ma) and zircon (24-19 Ma) fission-track (AFT and ZFT) ages from the Gangdese batholith just north of the Kailas basin. ZFT analysis of modern-river sand from the northern Gangdese magmatic arc indicates an exhumation at 27.3 ± 1.3 Ma. Thermal modeling indicates that the batholith experienced reheating between 28 and 20 Ma, coeval with deposition in the Kailas basin (between 26 and 21 Ma), followed by overall rapid cooling between 20 and 17 Ma. We interpret this thermal history as a phase of regional Oligocene-Miocene sedimentary burial followed by exhumation. By modeling mantle dynamics in the geodynamic framework of the India-Asia collision, we show that transient dynamic topography over the relative southward folding of the Indian slab is consistent with burial and exhumation of the Gangdese magmatic arc during Oligocene-Miocene time. The northward migration of the Indian continent relative to its own stationary slab created a wave of dynamic topography that caused subsidence in the overriding plate north of the Himalaya, followed by a phase of surface uplift since ~27 Ma of the northern Gangdese magmatic arc. During latest Oligocene-early Miocene time, the dynamic deflection center was in the Kailas area, and it progressively relocated southwards to its present position at the Ganges basin.

1 Introduction

The continent-continent collision between the Indian and Eurasian plates, following the northward movement of the Indian plate since the early Cenozoic, formed the Tibetan Plateau [*Dewey*, 1988; *Najman et al.*, 2010; *DeCelles et al.*, 2014; *Hu et al.*, 2016]. The orogenic deformation front has migrated both northward and southward from the initial collision zone at the Yarlung-Tsangpo suture zone [*Tapponnier et al.*, 2001; *Replumaz and Tapponnier*, 2003; *Yin*, 2010; *Kapp and DeCelles, 2019*]. In the center of this large Cenozoic continental collision zone, thick conglomerate layers were deposited during the Oligocene to Miocene and are exposed along strike to the north of the Indus-Yarlung suture zone with an east-west extension of more than 1000 km but with a north-south width of less than 10 km [*Heim and Gansser*, 1939; *Yin et al.*, 1999]. These rocks have been referred to as the Kailas Formation, named after the most famous holy mountain in Tibet, Mt. Kailas [*Cheng and Xu*, 1986], which is located in western Tibet and is composed of subhorizontal conglomerates [e.g., *Lacassin et al.*, 2004; *DeCelles et al.*, 2011]. The sediments of the current 6566-m-high peak have been buried to a depth of ~4-7 km during the early Miocene and have experienced significant exhumation at 17 Ma [*Carrapa et al.*, 2014]. In other places, the Kailas Formation experienced variable rates of accumulation, burial, exhumation and deformation [*Yin et al.*, 1999; *Sanchez et al.*, 2013; *Leary et al.*, 2016a]. Therefore, it could provide critical information for understanding the processes of India-Asian continental collision during the Cenozoic. However, the tectonic context of the conglomerates is still debated, with points of view including a foreland basin related to the southward-thrusting Gangdese Thrust (GT) [*Yin et al.*, 1999], a flexural basin associated with the termination or renewal of India-Asia collision [*Aitchison et al.*, 2007; *Wang et al.*, 2015], and an

extensional basin due to Indian slab rollback [*DeCelles et al.*, 2011; *Leary et al.*, 2016a]. The successive burial and exhumation processes in the early Miocene have highlighted significant uncertainty regarding the surface geological evolution and mantle dynamics in the collision zone since the Oligocene [e.g., *Replumaz et al.*, 2010; *DeCelles et al.*, 2011; *Husson et al.*, 2014; *Leary et al.*, 2016a; *Webb et al.*, 2017], which has renewed interest in the study of the geodynamics and mechanisms of the collision.

Disturbances in the subduction zone alter mantle flow, which in turn vertically deflects the surface of the Earth, thereby providing a simple mechanism to explain the formation of deep intracontinental basins [*Husson et al.*, 2014; *Webb et al.*, 2017]. This process is commonly referred to as dynamic topography: viscously flowing mantle imposes vertical stresses underneath the lithosphere, and these stresses are counterbalanced by a dynamic deflection of the surface of the Earth [*Husson et al.*, 2012]. In regions where the structure of the mantle quickly evolves (typically subduction zones), transient dynamic topography is expected to respond efficiently, and to be detectable in the geological record. Several theoretical [e.g. *Gurnis and Zhong*, 1991; *Husson et al.*, 2012] and case studies [e.g., *Husson*, 2006] point to kilometer-scale dynamic deflections in the topography above subduction zones. Such deflections are commonly transient, and the fast-changing Indian subduction dynamics are no exception. The northward motion of the Indian plate relative to its own slab [e.g. *van der Voo et al.*, 1999; *Replumaz et al.*, 2010] has been shown to be accompanied by a migration of the deflection above the mass anomaly in the mantle [*Husson et al.*, 2014]. At the surface, this process manifests as a southward-migrating wave of subsidence followed by a southward-migrating wave of uplift, already studied from the Himalaya towards the Ganges basin. These short-lived episodes explain both the Miocene surface uplift of the Himalaya and subsidence in the Ganges basin [*Husson et al.*, 2014; *Webb et al.*, 2017], as well as the formation of sedimentary basins on the NW Indian plate [*Najman et al.*, 2018]. This model offers a simple, single mechanism that explains a range of first-order observations. Thus, this interpretation represents an alternative to a more complex combination of processes involving removal of the mantle lithosphere [*Harrison et al.*, 1992; *Molnar et al.*, 1993], elastic flexure of the lithosphere [*Lyon-Caen and Molnar*, 1983], and extension triggered by slab rollback [*DeCelles et al., 2011; Leary et al., 2016a*].

In this paper, we further test the dynamic topography model by exploring whether the predicted southward-migrating waves of subsidence and uplift are recorded to the north of the Himalaya range and in southern Tibet. We revisit the spatial extent of the burial and exhumation experienced by the Kailas Formation and underlying rocks by reporting new in situ zircon fission-track (ZFT) and apatite fission-track (AFT) data and thermal modeling for the Gangdese batholith immediately to the north of the main preserved body of Kailas Formation rocks in the Mt. Kailas region in western Tibet. We focus on the succession of subsidence and exhumation and use numerical simulations to show that transient dynamic topography in response to mantle loading and unloading successfully reconciles structural, sedimentological, and thermochronological data in southern Tibet.

2 Geological settings

2.1 Regional geology

The Indus-Yarlung suture zone represents the site of the India-Asia continent-continent collision that began at ca. 60 Ma [e.g. *Najman et al.*, 2010; *DeCelles et al.*, 2014; *Hu et al.*, 2016] and separates the Lhasa terrane to the north and the Tethyan Himalaya to the south [*Yin and Harrison*, 2000]. Late Jurassic and early Cretaceous volcano-sedimentary rocks are widely distributed to the north of the suture zone in the Lhasa terrane and are related to the northward subduction of the Neo-Tethys oceanic lithosphere [*Zhu et al.*, 2011]. The Gangdese magmatic arc is located along the southern margin of the Lhasa terrane (Fig. 1) and is related to the end of oceanic subduction and removal of the slab at the onset of collision [e.g. *Mahéo et al.*, 2002, 2009]. This arc consists of the Linzizong volcanic rocks (with crystallization ages between ~65 and 45 Ma), the coeval Gangdese batholith (with crystallization ages between ~60 and 40 Ma) [*Harrison et al.*, 2000; *Mo et al.*, 2008, and references therein], and calc-alkaline and potassic-ultrapotassic volcanic rocks that formed in an Oligocene–Miocene stage [*Chung et al.*, 2005]. Some studies interpreted the last group of rocks as the products of a second slab breakoff, of the Indian lithosphere slab [e.g. *Mahéo et al.*, 2002, 2009]. Given the ages of the magmatic and volcanic rocks (K-Ar age of lamprophyres from the Karakorum range, NE Pakistan [*Rex et al.*, 1988], U-Pb and $^{40}Ar/^{39}Ar$ ages of adakitic volcanic rocks in western Tibet [*Miller et al.*, 1999; *Kapp et al.*, 2003; *Willams et al.*, 2004; *Gourbet et al.*, 2017], and the U-Pb age of an adakite in eastern Tibet [*Zhang L. et al.*, 2014], Fig. 1), breakoff is thought to have initiated at ~25 Ma at the western and eastern ends of the slab [e.g. *Replumaz et al.*, 2010; *Husson et al.*, 2014; *Webb et al.*, 2017].

The exhumation history of the Gangdese batholith has been highly debated over the past 20 years. In the eastern part of the batholith, near the city of Lhasa, $^{40}Ar/^{39}Ar$ thermochronological analyses have shown that the Gangdese batholith locally experienced two cooling stages, at 30-25 and 20-15 Ma [*Yin et al.*, 1999; *Harisson et al.*, 2000]. They have been interpreted as due to upper crustal thickening, in between the southward thrusting along the Gangdese Thrust (GT) (30-25 Ma) and northward thrusting along the Great Counter Thrust (GCT) (20-15 Ma), two major thrust faults described south of the Kailas Formation [*Heim and Gansser*, 1939; *Burg et al.*, 1987; *Ratschbacher et al.*, 1994; *Yin et al.*, 1994, 1999; *Kapp et al.*, 2007]. The north-dipping GT is mainly exposed along the eastern part of the Indus-Yarlung suture zone (between the Zedong and Xigaze) and was active during the Oligocene [*Yin et al.*, 1994, 1999]. The south-dipping GCT was active during 19-16 Ma [*Yin et al.*, 1999; *Harrison et al.*, 2000; *Laskowski et al.*, 2017] and juxtaposed rocks associated with the Tethyan Himalaya, Gangdese forearc basin and accretionary wedge atop the Gangdese magmatic arc and Kailas Formation [*Yin et al.*, 1999; *Murphy and Yin*, 2003]. Low-temperature thermochronological analyses (fission-track and (U-Th)/He) detected the second stage of cooling, which has been explained via a diverse range of interpretations, such as movement along the GT [*Copeland et al.*, 1995], surface uplift [*Carrapa et al.*, 2014; *Tremblay et al.*, 2015], and north-dipping duplex development beneath the Gangdese magmatic arc [*Laskowski et al.*, 2018].

In western Tibet, the dextral Karakorum strike-slip fault has been shown to be a transpressive flower structure, producing thrusting in the south of the Kailas basin. The fault is

connected to arc-perpendicular normal faults, such as the Xiao Gurla and Gurla Mandhata faults that have formed since ~15 to 9 Ma [e.g. *Murphy and Yin.*, 2003; *Lacassin et al.*, 2004; *Chevalier et al.*, 2005; *Valli et al.*, 2007; *Pullen et al.*, 2011; *Carrapa et al*., 2014; *Shen et al.*, 2016] (Fig. 1). Along the southern front of the Himalaya, sole thrusts are propagating towards the foreland, forming an orogenic wedge, and include duplex systems associated with the Main Central Thrust (MCT, active during the early Miocene), the Main Boundary Thrust (MBT, active during the late Miocene), and the Main Frontal Thrust (MFT, active during the Quaternary) [e.g., *Kohn et al.*, 2000; *Coutand et al.*, 2014] (Fig. 1).

2.2 Oligocene-Miocene sedimentary rocks deposition along the Gangdese magmatic arc

Deposition of the Kailas Formation to the south of the magmatic arc occurred earlier in the west (near the Kailas peak) between 26 and 21 Ma, between 25 and 22 Ma near Xigaze, and later eastward (near Zedong-Lhasa), between 23 and 18 Ma [*DeCelles et al.*, 2011, 2018; *Leary et al.*, 2016a; *Ai et al.*, 2019]. Detailed sedimentary analysis suggests that the formation in the Mt. Kailas area consists of a lower coarse-grained proximal conglomerate, a more distal fluvial sandstone member, a lacustrine shale and sandstone member, and an upper redbed clastic member [*DeCelles et al.*, 2011]. Most of the sediments were derived from the Gangdese magmatic arc to the north, with the exception of the uppermost redbed member [*DeCelles et al.*, 2011; *Leary et al.*, 2016a]. Previous study suggested that the Kailas basin was never more than 20 km wide [DeCelles et al., 2011]. However, several isolated outcrops of the formation are observed overlying the Gangdese batholith to the north of the present-day northern basin boundary (Fig. 2), indicating that the Kailas Formation extended farther north than previously thought [*Shen et al.*, 2019]. The layers near the Mt. Kailas area are nearly horizontal and the thickness of exposed stratigraphy is over 1500 m [*DeCelles et al.*, 2011; *Ai et al.*, 2019; *Shen et al.*, 2019]. AFT and zircon (U-Th)/He ages from the Kailas Formation at the depth of ~1000 m in the stratigraphic column near the Kailas peak are younger than the depositional age and require between 4 and 7 km of burial followed by rapid cooling and exhumation starting at 17 ± 1 Ma with a cooling rate of ca. 50 °C/Myr [*Carrapa et al.*, 2014]. The movement along the GCT deformed the southernmost fringe of the Kailas Formation [*Yin et al.*, 1999]. However, the subhorizontal stratigraphy of Mt. Kailas in the northern part of the basin also implies that crustal shortening and deformation have not affected the whole basin [e.g. *Lacassin et al.*, 2004; *DeCelles et al.*, 2011]. Further east in the Xigaze area, the Kailas Formation is ~1000 m thick [*Leary et al.*, 2016a], and a thermochronologic study also suggests burial between 4 and 7 km after the deposition according to a granite sample beneath ~900 m thick Kailas Formation [*Ge et al.*, 2018].

South of the Indus-Yarlung suture zone, in the central part of southern Tibet, deposition continued to the early Miocene with the Liuqu Formation exposed near Xigaze [*Li et al.*, 2015b; *Leary 2016*b] (Fig. 1). *Leary et al.* [2016b] suggested the Liuqu Formation represented a wedge-top basin of the northward thrusting of the GCT during or immediately after Indian slab breakoff, as contractional deformation resumed in the suture zone. However, clumped isotope thermometry of the Liuqu Formation revealed that it was buried between 2.9 and 3.3 km [*Ning et al.*, 2019], followed by rapid exhumation between 12-10 Ma [*Li et al.*, 2015b], indicating similar subsidence and uplift processes as for the Kailas Formation.

Oligocene-Miocene deposition to the north of the Gangdese magmatic arc has been little discussed so-far. The Rigongla Formation (Fig. 1), with alluvial fan, fluvial-channel and lacustrine facies, outcrops discontinuously at several locations within the central Lhasa terrane between Shiquanhe and Xigaze [*Wu*, 1979; *Kapp et al.*, 2003; *Zhu et al.*, 2006; *Zhao et al.*, 2011; *Wang et al.*, 2014; *Zhang K. et al.*, 2014; *Currie et al.*, 2016; *Gourbet et al.*, 2017; *Bai et al.*, 2018]. The Rigongla Formation consists overall of an over 500-m-thick fining-upward sequence of conglomerates, sandstones and mudstones derived from the surrounding Cretaceous volcanic rocks (interbedded dacite to andesite) [*Currie et al.*, 2016]. Dacites in the lower Rigongla Formation yielded a K-Ar age of 31.4 Ma [*Zhao et al.*, 2011; *Wang et al.*, 2014], providing a maximum age of deposition for the unit. Vitrinite reflectance values indicate that the rocks were buried to maximum temperatures of 95-125 °C [*Currie et al.*, 2016], corresponding to a depth between 3 and 4 km with an estimated thermal gradient of 30 °C/km.

2.3 Controversies associated with the formation of the Kailas basin

Several models have been proposed for the tectonic context of the Kailas basin deposition based on geological observations, all with major shortcomings or inconsistencies. *Yin et al.* [1999] suggest that the Kailas Formation was deposited in a foreland basin system related to the uplift and erosion of the Gangdese magmatic arc to the north of the basin. The basin was uplifted by the top-to-the-south GT below the batholith, which is blind in the Kailas region but emergent to the east in the Zedong region, possibly active between ~31 and 24 Ma [*Yin et al.*, 1999; *Harrison et al.*, 2000]. Both the absence of the GT in the Mt. Kailas region and the proposed timing for the onset of the fault (5 Ma earlier than the deposition of the Kailas Formation) argue against this model. *Wang et al.* [2015] proposed another compressional model, which interpreted the basin as a flexural foredeep basin loaded, to the south in this case, by the top-to-the-north GCT, which bounded the basin to the south. However, the onset of the GCT (19-16 Ma) after the main deposition phase of the Kailas Formation (26-21 Ma), as well as the northern provenance of the sediments, challenge this interpretation [*DeCelles et al.*, 2011; *Laskowski et al.*, 2017].

Finally, based on sedimentary and thermochronology studies, it has been suggested that the Kailas Formation was deposited in an extensional context during relative southward rollback of the Indian slab below southern Tibet prior to Miocene slab breakoff [*DeCelles et al.*, 2011; *Carrapa et al.*, 2014; *Leary et al.*, 2016a; *Laskowski et al.*, 2017; *Webb et al.*, 2017]. In this model, the northern edge of the Indian slab reached the northern Lhasa terrane between 30 and ~26 Myr ago [*DeCelles et al.*, 2011; *Kapp and DeCelles*, 2019]. The subsequent, long-range slab rollback is interpreted to be represented by a coeval southward migration of volcanism across the Lhasa terrane. During sediment deposition, the Kailas basin would have been bounded to the south by a normal fault and was later disrupted by thrusting on the GCT. The Kailas basin was then subsequently exhumed in response to renewed Indian plate underthrusting following slab detachment. However, at the scale of the Tibetan plateau, there are only three volcanic belts [*Chung et al.*, 2005], which have been interpreted as related to subduction events. The main belt is the Gangdese magmatic arc following the Indus-Yarlung suture, related to the northward subduction of the Indian plate. Another belt is following the Jinsha suture, related to the southward subduction of the Asian lithosphere in an early phase of collision [e.g. *Horton et al.*, 2002; *Spurlin et al.*, 2005; Goussin et al., 2020]. Finally, one belt follows the Kunlun suture, related to on-going southward Asian lithosphere subduction since ~15 Ma (Fig. 1). In between the Indus-Yarlung and the Jinsha sutures, volcanism is sparse in the Qiangtang and the Lhasa

terranes, where its spatial pattern does not appear consistent with a continuous southward migration wave associate to a slab-roll-back (Fig. 1). Furthermore, this scenario relies on unsupported geodynamic and structural inferences and unlikely mechanical behavior. Structurally the extensional setting is only indirectly inferred from the large-scale architecture of the basin, which is interpreted as growth-strata. No clear evidence of normal faulting is reported [*Leary et al*., 2016a]. The mechanical impact of slab rollback within a sustained collisional setting, as advocated in this model, may be misinterpreted. While the slab continued to roll back during the deposition of the Kailas Formation, the still-converging Indian and Eurasian plates sustained compression in the Himalaya, and potentially caused extension in the mantle wedge above the slab. Only compression – not extension – is expected between the colliding lithospheres [*Replumaz et al.*, 2016; *Pitard et al.*, 2018]. Therefore, both the absence of unambiguous extensional structures and a problematic geodynamic framework weakens this interpretation.

3 Thermochronology

3.1 Samples and dating results

We collected six bedrock samples from the Gangdese batholith along two transects, one 20 km and another ~80 km east of Mt. Kailas (Fig. 2), for AFT, ZFT and zircon U-Pb dating. Detailed analytical procedures for zircon U-Pb, ZFT and AFT dating are presented in the Supporting Text S1. The zircon U-Pb ages are 41.0 ± 1.1 Ma (13T02) and 50.8 ± 1.6 Ma (14T05) (see Table S1 for details), with Pb/U concordia diagrams created using Isoplot (v. 3.75) [*Ludwig*, 2012] shown in Figure 3. ZFT analysis yielded cooling ages between 19.6 ± 2.0 and 24.1 ± 3.3 Ma (±2σ) (Table 1), and AFT analysis yielded cooling ages between 16.3 ± 1.9 and 11.5 ± 2.1 Ma (±2σ) (Table 3). Detailed fission-track data are provided in the Appendix A1. These ages do not show significant correlation with sample elevation (Fig. 4A). For samples 13T01 and 13T02, 135 and 77 apatite confined track lengths are measured (Table 3), providing mean AFT c-axis projected length of 13.89 ± 1.32 and 13.74 ± 1.38 μm (with 1 standard deviation), respectively. The samples 14T01 and 14T05 each yielded less than 50 measured track lengths, with mean values of 14.22 ± 1.09 and 14.59 ± 1.14 μm.

One modern river sand sample was collected to the north of the Gangdese magmatic arc, approximately 90 km east of Shiquanhe (Fig. 5), and subjected to ZFT analysis. The river originated from the Mt. Kailas area to the south, running mostly northward through the Linzizong volcanic rocks and belonging to the Indus drainage system. The Linzizong volcanic rocks cover most of the drainage area; therefore, the sediment sample could be used to reveal the long-term exhumation history of the Linzizong volcanic rocks in the northern part of the Gangdese magmatic arc. Central and peak ages of the sample are determined and plotted with the RadialPlotter by *Vermeesch* [2009] and presented in Table 4 and Fig 5. The detrital ZFT grains ages range from 15.0 to 96.0 Ma, and three peak ages of 27.3 ± 1.3, 40.5 ± 2.3 and 70.0 ± 8.1 Ma are obtained.

3.2 Thermochronological modeling

Fission-track data, including AFT ages, AFT lengths and ZFT ages, are modeled using the QTQt software (v. 5.5.0) [*Gallagher*, 2012] to extract thermal history models. We only performed modeling for samples from the western transect (sample 13T series) because samples from the other transect provided insufficient AFT length data for modeling. The two zircon U-Pb ages from the Gangdese batholith of 41.0 ± 1.1 Ma (13T02) and 50.8 ± 1.6 Ma (14T05), interpreted as the age of the batholith intrusion and crystallization, have been introduced into the model as a thermal constraint of 750 ± 100 °C [*Harrison et al.*, 2007; *Valley et al.*, 2006] between 50 and 40 Ma. The fact that the Kailas Formation was deposited unconformably on the granite means that the top of the batholith was at the surface before deposition started, i.e., at ~26 Ma at the location of the Kailas basin [*DeCelles et al.*, 2011]. This condition has been introduced as a second thermal constraint with a low temperature (0-400 °C) between 32 and 26 Ma to take into account the shallow depth range of the samples before Kailas Formation deposition (Table 1 and Fig. 4B) and the present-day surface temperature of 0 ± 10 °C (mean annual surface temperature from 1961 to 2000 on the Tibetan Plateau, *Yang et al.* [2010]).

After discarding the initial 50,000 burn-in iterations, 200,000 iterations of the model are run. For fission-track annealing kinetics, the multi-kinetic annealing model of [*Ketcham et al.*, 2007] was chosen for AFT data, and the kinetics of *Yamada et al.* [2007] are chosen for ZFT data. Compositionally dependent initial track lengths are calculated based on a Dpar value for each apatite grain, calibrated against the Durango apatite standard. Detailed QTQt modeling parameters are shown in Table 1, and all the data used for QTQt modeling are shown in Supplementary Table S2. The Eocene post-magmatic cooling is constrained by the two thermal constraints imposed on the model, resulting in rapid cooling between ~40 Ma and ~28 Ma, compatible with the published K-feldspar $^{40}Ar/^{39}Ar$ age of 31.33±0.26 Ma (Fig. 4A) from the nearby granite sample 95-6-11 (Fig. 2) [*Yin et al.*, 1999]. For the fission track data, the best fit inversion model obtained with QTQt shows a 3-stage thermal history (Fig. 4B): 1) heating from ~200 °C (60-350 °C with 95% confidence interval) to ~380 °C (320-420 °C with 95% confidence interval) between ~28-26 and ~20 Ma (16-40 °C/Myr), 2) rapid cooling from ~380 °C (320-420 °C with 95% confidence interval) to ~100 °C (30-120 °C with 95% confidence interval) between 21-20 and 17 Ma with a minimum cooling rate of ~50 °C/Myr , and 3) relatively slow cooling since ~6 Ma after a ~10 Myr residence time in the AFT partial annealing zone. The model-predicted ages and track length are plotted in Figure 4C, and the individual sample predictions by QTQt are provided in Appendix A2.

4 Dynamic topography modeling

We modeled changes in dynamic topography to decipher the link between first-order geomorphic changes and deep slab movements. We model the viscous flow beneath the Indian-Eurasian convergence zone following the Stokeslets approximation [*Morgan*, 1965; *Harper*, 1984], which has proven successful in global [e.g. *Ricard et al., 1993*] and more regional [*Guillaume et al.*, 2009] models. The density field is discretized into point masses, and each point mass *i* induces an elementary flow for which the stream function is known [e.g. *Batchelo*r, 1967], which can be written as follows:

$$\Psi_i = \frac{\Delta\rho v_i g}{8\pi\eta} r_{ij} \sin^2 \theta_{ij}$$

where $\Delta\rho v_i$ is the mass anomaly associated with each point mass, g is the acceleration of gravity, η is the viscosity, r_{ij} is the distance from the point mass i to a point j at the surface, and θ_{ij} is the angle between the vector ij and g. The normal stress is computed following the image technique, as in *Morgan* [1965]:

$$F_{ij} = \frac{3\Delta\rho v_i g z_i^3}{\pi r_{ij}^5}$$

where z_i is the depth of the point mass. For a stress-free surface, the normal stress is compensated by an opposite surface load. That surface load is a deflection of the surface (dynamic topography):

$$h_{ij} = \frac{F_{ij}}{(\rho_m - \rho)g}$$

where ρ_m is the density of the mantle and ρ is the density of water in immersed domains, air in subaerial domains (as in the Himalaya for instance) or sediments in sedimentary plains (such as the Indo-Gangetic plain). The total deflection H_{ij} is the sum of all individual deflections, and the dynamic topography at a given location is given by the following:

$$H_{ij} = \frac{3\Delta\rho v_i g z_i^3}{\pi r_{ij}^5 (\rho_m - \rho)}$$

Here, we take advantage of this semianalytical formalism to explore the dynamic topography (as in *Husson* [2006]) above a flowing mantle around reconstructed idealized slab geometries.

We computed models of dynamic topography from our reconstructed geometries at intervals of 5 Myr, and only updating the slab geometry between 30 and 25 Ma in order to account for shortening and slab relocation beneath the Himalaya. Slab geometries at each time are reconstructed as described in *Husson et al.* [2014] and *Webb et al.* [2017], based on geophysical observations for present-day, and geological arguments for past reconstructions in the past complemented by lessons from numerical and analogue models. In practice, slab geometries are simplified as down-dipping surfaces. Slabs are linear at the surface and distorted at depth. That distortion is defined by a laterally variable dip along the trench. Over time, the slab overall rotates from a north-dipping to a south-dipping slab over 25 Myr period. In addition, the slab gradually detaches from the edges towards the center over the same period. Last, the slab is offset with respect to the trench, by an amount that decreases over time, to account for relative rollback. Detailed geometries are accessible in *Husson et al.* [2014].

Slabs at each time step are discretized into individual Stokeslets (or point masses). The negative buoyancy of the slab at any time is computed assuming that an unstretched section of slab has a thickness of 110 km and a density contrast with the mantle of 60 kg m^{-3}. The total buoyancy of the slab in the upper mantle is assumed to be uniform per unit trench length at each time step. Because the lithosphere stretches as it gets closer to the edges, its thickness decreases. Thus, the absolute buoyancy of the individual point masses decreases, and we adjust the values

accordingly. In these models, we only consider the density anomaly of the slab; hence, the net density anomaly is positive. This implicitly corresponds to the assumptions that opposing buoyancy anomalies (to restore a neutral net buoyancy) are either uniformly distributed in the mantle or too remotely located to produce any effect in the area. In both cases, there is no impact on the model predictions. Summing up individual flows of each Stokeslet yields the entire flow, from which the vertical stress beneath the surface can be computed.

The vertical stress is compensated by a long-wavelength (100s of km) deflection, either filled with air, sediments, or water. This is critical because the magnitude of the deflection scales with the density contrast between the mantle and the filling material, namely, sediments in the Indo-Ganges plain and Kailas basin (corresponding to a density contrast of 500 kg m^{-3}) and air in the Himalayan belt (corresponding to a density contrast of 3200 kg m^{-3}). Note that the deflection has a very low aspect ratio (amplitude over wavelength) which implies that its geometry remains insensitive to the elasticity of the lithosphere, regardless of its compensation. We therefore predict air-compensated deflections δza and sediment-compensated deflections δzs (and their temporal variations, i.e., uplift and subsidence; Fig. 6). Because air-compensated topographic change by default assumes no erosion, we also computed the values of surface uplift with an amount of equivalent erosion in order for the elevation to remain constant throughout while maintaining isostasy. This scenario represents the maximum bound for bulk exhumation of the Gangdese batholith and Kailas basin caused by dynamic surface uplift.

As the slab remains stationary underneath the northward-drifting Indian plate, our model predicts a wave of dynamic subsidence migrating from the Lhasa terrane to the south (from ~30 to 26 Ma, Fig. 6) towards its current southern location, where it now explains the deflection of the foreland basin (see also *Husson et al.* [2014]). If compensated by sediments, as we hypothesize for the Kailas basin, the predicted deflection amounts to about 4 to 7 km (note that it would be only ~1 km in the absence of sedimentary infill, i.e., if the stresses were compensated by air instead of sediments). As the slab migrates southward relative to the Himalaya, the mantle load and dynamic deflection relocate southward and the topography bounces back. In the absence of erosion, our model predicts a surface uplift of ~1 km. If this surface uplift were instantaneously compensated by erosion, the amount of rock uplift could be as high as 5-6 km.

5 Discussion: dynamic subsidence and surface uplift in southernmost Tibet

Multiple unrelated processes have been invoked in the past to explain several observations of vertical land motion that cannot be explained by horizontal shortening or extension. Classic examples include the mid-Miocene uplift of southern Tibet and the Himalaya and the coeval onset of rapid deposition of the Siwalik series in the foreland basin. Canonical explanations involve removal of the mantle lithosphere [e.g., *Harrison et al.*, 1992; *Molnar et al.*, 1993] and elastic flexure of the lithosphere [e.g., *Lyon-Caen and Molnar*, 1983]. While each process is independently mechanically plausible, they are somewhat incompatible: if lithospheric unloading by removal of the lithospheric mantle in southern Tibet is invoked to explain the mid-Miocene uplift of southern Tibet and the High Himalaya, it implies that the vertical load exerted by the overriding lithosphere decreases. Removing the dense mantle lithosphere would counteract the overloading effect of the thickened crust and the net result would arguably be to unload the overriding lithosphere. The flexural response of the subducting plate would adjust accordingly, and the unloaded overriding lithosphere would be incapable to increase the

deflection, but would perhaps decrease it. It follows that if delamination prevails in the upper plate, it therefore simultaneously rules out the lithospheric flexure hypothesis under an increased load at the plate boundary to explain the synchronous development of the foreland basin. In contrast, transient dynamic topography is a simple mechanism that provides a single explanation for these first-order observations. Here, we show that deposition and erosion of the Kailas Formation in the southern Lhasa terrane are further evidence of the same process.

Other explanations [e.g., *Wang et al.*, 2015] invoke elasticity in the upper plate. Such a model would work if elasticity could prevail over long time scales (i.e., that of an orogen). We deem this hypothesis unlikely because the tectonically disrupted lithosphere and the high thermal regime suggest that viscous relaxation should quickly take over. Importantly, our model is conversely insensitive to the elasticity of the upper plate; the dynamic deflection only owes its origin to viscous fluxes in the mantle, and its cessation to the release of the viscous traction underneath the surface. The subsequent rebound (Fig. 6) is not due to any elastic rebound, but only to the restoration of isostatic equilibrium.

5.1 Transient subsidence across the Lhasa terrane

The best-fit line of thermal history shows the granites of the Gangdese batholith north of the Kailas basin after crystallization (50-40 Ma), began with a cooling to ~200 °C (60-350 °C with 95% confidence interval) during ~40 to ~28 Ma followed by a reheating phase between 28-26 and 21-20 Ma with temperature increasing to 320-420 °C, in the Kailas area (Fig. 4B). This reheating is coeval with the heating of the Kailas Formation during its deposition between ~26 and ~21 Ma [*Carrapa et al.*, 2014], suggesting that both the deeper sedimentary rocks of the basin and the underlying batholith were heated by the burial below thick sedimentation in a rapidly subsiding basin. Such burial is in agreement with our inversion of the thermal data showing that the batholith has been reheated to temperatures in excess of 320-420 °C (Fig. 4B). This implies that subsidence was not restricted to the present-day exposure of the Kailas basin but spanned a broader region including the current Gangdese batholith exposures, which also experienced burial. Isolated exposures of conglomerates atop the batholith (Fig. 2) have been interpreted as local remnants of such a more extended Kailas Formation [*Shen et al.*, 2019] (Fig. 2).

Our dynamic models show that the southward-migrating wave of dynamic topography implies a phase of dynamic subsidence. The initiation of deposition could have occurred north of the Gangdese magmatic arc south of the Lhasa terrane above the Indian slab, subducted since ~35 Ma after the Neo-Tethyan slab breakoff at ~45 Ma [*Guillot et al.*, 2003; *Replumaz et al.*, 2014]. The deposition of the Rigongla Formation at ~31 Ma along the northern margin of the Gangdese magmatic arc between Shiquanhe and Xigaze could correspond to this initial subsidence (Fig. 6A). Dynamic topography modeling estimates subsidence amounting to ca. 4 km, compatible with the amount of sediment thickness between 3 and 4 km estimated for Rigongla Formation in Namling [*Currie et al.*, 2016]. Afterwards, subsidence migrated southwards as the northward-drifting Indian plate moved above its own stationary slab, leading to an overturned geometry (Fig. 6). During the Oligocene to Miocene (between 26 and 21 Ma), subsidence occurred in the Gangdese magmatic arc and Indus-Yarlung suture zone, yielding a maximum subsidence of ~ 6 km between the magmatic arc and suture zone (Fig. 6B). The current extent of the Kailas basin probably represents the location of the depocenter, which

experienced ca. 4-7 km of burial [*Carrapa et al.*, 2014], and the magnitude of burial shallowed northward, with ca. 4 km of burial in the Gangdese batholith according to our thermal modeling (Fig. 6B). Moreover, according to the thermal model in this study, the 16-40 °C/Myr heating rate is compatible with a sediment accumulation rate of 0.5-1.3 km/Myr, which is consistent with the 4-7 km burial during 26-21 Ma at a deposition rate of 0.8-1.4 km/Myr [*Carrapa et al.*, 2014].

Importantly, the dynamic deflection did not create the basin by itself: the southward increase in mantle traction during sedimentation only manifested as a southward tilt of the upper plate. For the deflection to be filled by water and sediments at an elevation of 1500-2900 m above sea level [*DeCelles et al.*, 2011; *Ai et al.*, 2019], the basin thus needed to be capable of storing sediments. This inference implies that the dynamic deflection could be recorded only in sedimentary basins in which the outlets of the drainage system were partly hindered by surrounding topographic highs (Fig. 7 A and 7B). Indeed a paleoaltitude analysis has suggested that the Gangdese magmatic arc was slightly higher (~4500 m) than the area to the north (<3000 m) [*Ding et al.*, 2014], which provided ideal conditions for the deposition of the Rigongla Formation (Fig. 6A). South of the Indus-Yarlung suture, even though the Himalaya range had not reached its highest elevations [*DeCelles et al.*, 2011, 2018; *Ai et al.*, 2019], the sediments deposited in the foreland basin in Nepal during the Oligocene [*DeCelles et al.*, 2004; *Najman et al.*, 2005], are indicative of some relief in the Himalaya, with elevation exceeded 3600 m at the late Miocene [*Chen et al.*, 2020]. These ranges could have circumscribed an interior drainage system around the Kailas basin (Fig. 7B). It follows that the dimensions of the Kailas basin were not exclusively set by the dynamic deflection itself but also by the elevations of the drainage outlets with respect to the depocenter. This difference in elevation dictated the thickness of the sedimentary layer that could be deposited at that time and, consequently, the extent of the Kailas basin in all directions. Geometrically, the basin thickens southward towards the Himalaya. This is attested by the fan-shape of the formation, which has previously been interpreted as growth strata [e.g. *Leary et al., 2016a*]. These rare conditions for sediment storage (instead of sediment export) explain why the extent of the sedimentary basin (possibly up to a maximum north-south width of 50 km at the time of deposition) is much narrower than the bulk dynamic deflection (several 100s of km) (Fig. 7B and 7 D). Additionally, the dynamic deflection not only caused subsidence but also the subsequent uplift (see following section), which means that with the southward migration of the deflection, uplifted areas to the north would be exhumed and eroded, which provided sediments southward to the subsided Kailas basin. This implies the formation of proximal sedimentary facies in the subsiding basin, at least along its northern margin, is consistent with the alluvial fan lithofacies of the Kailas Formation in the early stage [*DeCelles et al.*, 2011]. Moreover, the ZFT peak age of the modern river sand from the central Lhasa terrane suggests that the volcanic rocks to the north of the Gangdese magmatic arc experienced exhumation at ~ 27.3±1.3 Ma (Fig. 5). This timing is coincident with the initial reheating of the Gangdese batholith to the south according to the thermal modeling (Fig. 4) and with the subsequent deposition in the Kailas basin. Volcanic gravel clasts, not granite, dominate the conglomerate clasts in the Kailas Formation, further indicating that the main source of the sediments was the Linzizong volcanic rocks to the north, not the Gangdese batholith [*DeCelles et al.*, 2011; *Shen et al.*, 2019]. Sedimentation ceased when the efficient river incision and evacuation of material from southern Tibet by the paleo-Yarlung River and Indus River occurred during the early to middle Miocene [*Carrapa et al.*, 2017].

5.2 Middle Miocene uplift in southern Tibet

The period of subsidence in the sampled region was followed by a period of exhumation between 20 and 17 Ma. Considering a thermal gradient of 30 °C/km during this exhumation phase, the cooling is estimated to correspond to a minimum of 6.6 km of exhumation (6.6-13 km considering 95% confidence interval, according to the thermal model) (Fig. 4). Similar magnitudes of exhumation are recorded during the same time interval across the Ladakh batholith [*Kirstein et al.*, 2006], Kailas basin [*Carrapa et al.*, 2014], Gyirong basin [*Shen et al.*, 2016], Xigaze area [*Dai et al.*, 2013*; Ge et al.*, 2017, 2018] and eastern Tibet [*Tremblay et al.*, 2015; *Li et al.*, 2015a] (Fig. 1 and 8). The elevation of southern Tibet was still relatively low (1500-2900 m) during the time of deposition (26-21 Ma) of the Kailas Formation [*DeCelles et al.*, 2011, 2018; *Ai et al.*, 2019], while after the phase of exhumation (20-17 Ma) the Namling basin attained elevations of approximately 4000 m [*Spicer et al.*, 2003]. Moreover, no major thrust faults or major deformation events are observed to be directly associated with the surface uplift of the Kailas basin, which lies in the footwall of the GCT, rests unconformably on the Gangdese batholith to the north (Fig. 2), and has a well-preserved, seemingly isopachous stratigraphy [e.g. *Yin et al.*, 1999]. Besides, the rapid river incision along the Yarlung-Tsangpo River mainly occurred after 15 Ma and was almost confined at the east of the Xigaze area [e.g., *Rohormann et al.*, 2012; *Dai et al.*, 2013; *Li et al.*, 2015a], so that it also cannot account for the exhumation between 20 and 17 Ma across the southern Tibet.

In the absence of clear evidence for horizontal tectonics, our dynamic model provides an explanation. Once the downward deflection associated with the slab migrated to southern locations, the topography uplifted towards an isostatically compensated elevation (Figs. 6B and 7A). The wave of surface uplift first occurred in the northern Gangdese magmatic arc, according to the young ZFT peak age of modern river sand from the central Lhasa terrane, showing exhumation at ~ 27.3±1.3 Ma (Fig. 5), then migrated southward. As the deflection migrated south of the Kailas basin it first starved then eventually exhumed and eroded from 20 Ma onwards, while subsidence started in the Himalayan foreland basin (Figs. 6C and 7C). Topographic subsidence may have bypassed the Himalaya itself, or was perhaps diminished across the range. This could occur due to development of the orogenic wedge (i.e., the MCT active during the early Miocene, the MBT active during the late Miocene, and the MFT active during the Quaternary [e.g., *Kohn et al.*, 2000; *Coutand et al.*, 2014]), such that tectonic shortening and concomitant crustal thickening (e.g., duplex systems) could have compensated for the otherwise predicted topographic deflection [*Webb et al.*, 2017]. Further exploration of the impacts of the relative southwards motion of the slab on the thrust tectonics, topography, and climate across the Himalayan orogenic wedge are presented in *Webb et al.* [2017].

The model-predicted dynamic surface uplift amounts to approximately 1 km. This value is consistent with the estimated increase in elevation before and after rock cooling, according to fossil leaf evidence, which suggested a 1500-2900 m elevation for the Kailas basin at ~23 Ma [*Ai et al.*, 2019] and a 4638±847 m elevation for southern Tibet at 15 Ma [*Spicer et al.*, 2003]. The associated exhumation rates can be computed, to the first order, by assuming that isostatic equilibrium is restored when the elevation remains constant. This yields at maximum approximately 6 km of exhumation (Fig. 6C), which is comparable to data from the Gangdese batholith. This exhumation was accompanied by intense surface erosion, reducing the present-day preserved thickness of the Kailas Formation [*DeCelles et al.*, 2011, 2018] (Fig. 7D). In

practice, exhumation does not strictly result in a constant elevation, and some of the surface uplift is not compensated by erosion. The remainder has uplifted the Kailas basin in southern Tibet from its basin surface elevation during deposition (1500-2900 m), to its modern elevation of 4500-6700 m.

5.3 Along-strike dynamic deflection

Along the Himalayan arc, the present-day dynamic deflection center (more than 6 km of sediment compensated deflection in the foreland) is located in the middle of the range, with no deflection below the eastern syntaxis, and a smaller amplitude to the west (-2 km), as shown by *Husson et al.* [2014] (Fig. 8A). It is due to the geometry of the slab, whose center of mass is located below the middle of the Himalayan range along the arc-parallel direction [e.g. *Replumaz et al.*, 2010, 2014]. It has been similar since the Miocene time, with about 8 km of sediments deposited in the middle of the foreland basin along the arc-parallel direction, and less than 1 km close to the eastern and western syntaxes [*Husson et al.*, 2014, and references therein].

Thermochronologic data reveal a similar longitudinal pattern for the Kailas formation, whose depocenter was located above the center of mass of the subducting slab, in the middle of the suture in the arc-parallel direction (Fig. 8A). In the Mt. Kailas area, rapid exhumation occurred at ca. 20-17 Ma for the Kailas Formation [*Carrapa et al.*, 2014] with AFT ages mostly younger than ~20 Ma (Fig. 8B). To the east, in the Xigaze area, rapid exhumation occurred at ca. 16-14 Ma for the Kailas Formation [*Ge et al.*, 2018] and 16-10 Ma for the Liuqu Formation [*Li et al.*, 2015b], with also AFT ages younger than ~20 Ma (Fig. 8C). Between the Kailas Formation to the north and the Liuqu Formation to the south, the rocks from the Xigaze basin also experienced rapid exhumation at ca. 16-15 Ma showing < 20 Ma AFT (Fig. 8C) [*Li et al.*, 2017].In the Zedong area, thermal modeling also suggests rapid exhumation at 20-17 Ma for the Kailas Formation with AFT ages younger than 20 Ma [*Li et al.*, 2015a] (Fig. 8 D). These thermochronologic data suggest all the late Oligocene to early Miocene deposits exposed south of the Gangdese magmatic arc have been experienced rapid exhumation around 20-15 Ma. However, the AFT ages of the Gangdese batholith are not fully confined to younger than 20 Ma, except in the Mt. Kailas area (this study) (Fig. 8B). In the Xigaze area, granitic rocks located ~50 km north of the suture zone have AFT cooling ages at around 25 Ma, and the <20 Ma ages are mostly limited close to the Kailas Formation (Fig. 8C). The AFT ages of granitic rocks in the Zedong area are scatter from 60 to 15 Ma and most of them are older than 20 Ma (Fig. 8D), indicating that the cooling ages of these granitic rocks were not reset by the deposition of the Kailas Formation probably due to shallow burial. This lack of young ages to the east of Tibet (Fig. 8) and of the Himalaya [*Webb et al.*, 2017], corresponding to a low amount of sedimentation in the Ganges basin (Fig. 8A), suggests that the dynamic deflection center was in the Mt. Kailas area during the deposition of the Kailas formation (26-21 Ma) and in the Ganges basin (since 15 Ma) [*Husson et al.*, 2014]. The maximum of dynamic deflection result in deep subsidence and rapid uplift of both the Kailas Formation and the Gangdese batholith. To the east, the relatively old cooling ages of the Gangdese batholith and the young cooling ages of the Kailas Formation indicate shallow burial and reduced width of the Kailas Formation, implying a relatively small amplitude of deflection.

6 Conclusions

Geodynamic models attempting to explain the India-Asia collision process must incorporate a mechanism that allows the southern fringe of the upper plate plateau to be topographically depressed during collision. Our new thermochronological data and modeling of samples from the Gangdese batholith in southwestern Tibet illustrate that not only the Kailas basin but also over a relatively large region in southern Tibet was topographically depressed. After being exposed at the surface, the Gangdese batholith experienced reheating during burial beneath the Kailas Formation between ~28-26 and 21-20 Ma, followed by rapid cooling between 20 and 17 Ma. This thermal history is compatible with the results of dynamic topography modeling based on mantle dynamics. We show that the northward migration at the surface of the Indian continent above its own stationary slab, induced a wave of dynamic topography, accompanied by a phase of subsidence in southern Tibet followed by a phase of uplift, as the dynamic deflection migrated southward to the Ganges basin. The computed estimate of the dynamic topography in the upper plate predicts approximately ~4 km of dynamic subsidence, followed by ~6 km of exhumation and 1 km of surface uplift in the southern Gangdese batholith, which are compatible with sedimentary and thermochronology observations.

The large-scale accumulation of sediments in the Kailas basin required conditions in which the sediments were not entirely transported out of the system by rivers at that time. The rivers draining the Gangdese batholith to the south did not cross the Himalaya range, which was rising during this period, thus providing the rare conditions necessary to block sediments in the interior of this elevated region. In fact, the very existence of the Kailas basin is itself surprising: dynamic deflection alone is not sufficient; the sediments must have been able to settle instead of being washed out. The Kailas basin is thus perhaps the unique occurrence of a perched basin that owes its existence to dynamic topography, which temporarily offered the appropriate conditions for sediment storage, while most intermontane basins are likely explained by lateral variations of crustal tectonics.

Acknowledgments

This work has been supported by National Natural Science Foundation of China (41702208 and 41672195), and the China Geological Survey (Grant Nos. 1212011121261). Bowen Song, Junliang Ji, Keke Ai, and Gaolei Jiang provided support during fieldwork. Melanie Balvay is acknowledged for help during the AFT and ZFT sample preparation. We also thank the suggestions by Djordje Grujic, Feng Cheng, Jonas Ruh, Giuditta Fellin, Barbara Carrapa, Devon A. Orme, Andrew Laskowski, and Peter G. DeCelles which helped to significantly improve the manuscript. All the new thermochronological data are archived in Figshare repository (https://doi.org/10.6084/m9.figshare.11626053.v1).

References

Ai, K., G. Shi, K. Zhang, J. Ji, B. Song, T. Shen, and S. Guo (2019), The uppermost Oligocene Kailas flora from southern Tibetan Plateau and its implications for the uplift history of the southern Lhasa terrane, Palaeogeography Palaeoclimatology Palaeoecology, 515, 143-151, doi:10.1016/j.palaeo.2018.04.017.

Aitchison, J.C., J.R. Ali, and A.M. Davis (2007), When and where did India and Asia collide? Journal of Geophysical Research, 112, B05423, doi: 10.1029/2006JB004706.

601 Bai, P., X. Xiong, Y. Zeng, D. Ma, H. Fu, Y. Li, K. Jiang, H. Zhang, T. Wu, J. Huang and Z.
602 Liao (2018), The discovery and significance of the sporopollen assemblages from the
603 Oliogene Rigongla Formation in the Lunggar region Zhongba Xizang, Sedimentary
604 Geology and Tethyan Geology, 38(3), 70-76.

605 Batchelor, G. (1967), An Introduction to Fluid Mechanics, Cambridge University Press.

606 Burg, J.-P., A. Leyreloup, J. Girardeau, and G.-M. Chen (1987), Structure and metamorphism of
607 a tectonically thickened continental crust: The Yalu Tsangpo suture zone (Tibet),
608 Philosophical Transactions of the Royal Society of London, ser. A, 321, 67–86, doi:
609 10.1098/rsta.1987.0005.

610 Carrapa, B., D. A. Orme, P. G. DeCelles, P. Kapp, M. A. Cosca, and R. Waldrip (2014),
611 Miocene burial and exhumation of the India-Asia collision zone in southern Tibet:
612 Response to slab dynamics and erosion, Geology, 42(5), 443-446, doi:10.1130/g35350.1.

613 Carrapa, B., M.F. bin Hassim, P.A. Kapp, P.G. DeCelles, and G. Gehrels (2017), Tectonic and
614 erosional history of southern Tibet recorded by detrital chronological signatures along the
615 Yarlung River drainage, Geological Society of America Bulletin, 129 (5-6), 570–581.

616 Chapman, J. B., and Kapp, P. (2017). Tibetan magmatism database. Geochemistry, Geophysics,
617 Geosystems, 18, 4229-4234.

618 Chen, C., Y. Bai, X. Fang, Q. Xu, T. Zhang, T. Deng, J. He and Q. Chen (2020), Lower-altitude
619 of the Himalayas before the mid-Pliocene as constrained by hydrological and thermal
620 conditions, Earth and Planetary Science Letters, 545, 116422.

621 Cheng, J., and G. Xu, (1986), Geologic Map of the Gaize Region with Report: Tibetan Bureau of
622 Geology and Mineral Resources.

623 Chevalier, M. L., F. J. Ryerson, P. Tapponnier, R. C. Finkel, J. Van der Woerd, H. B. Li, and Q.
624 Liu (2005), Slip-rate measurements on the Karakorum Fault may imply secular variations
625 in fault motion, Science, 307(5708), 411-414, doi:10.1126/science.1105466.

626 Chung, S. L., M. F. Chu, Y. Q. Zhang, Y. W. Xie, C. H. Lo, T. Y. Lee, C. Y. Lan, X. H. Li, Q.
627 Zhang, and Y. Z. Wang (2005), Tibetan tectonic evolution inferred from spatial and
628 temporal variations in post-collisional magmatism, Earth-Science Reviews, 68(3-4), 173-
629 196, doi:10.1016/j.earscirev.2004.05.001.

630 Copeland, P., T. M. Harrison, P. Yun, W. S. F. Kidd, M. Roden, and Y. Q. Zhang (1995),
631 Thermal evolution of the Gangdese batholith, southern Tibet - a history of episodic
632 unroofing, Tectonics, 14(2), 223-236, doi:10.1029/94tc01676.

633 Coutand, I., D. M. Whipp, D. Grujic, M. Bernet, M. G. Fellin, B. Bookhagen, K. R. Landry, S.
634 K. Ghalley, and C. Duncan (2014), Geometry and kinematics of the Main Himalayan
635 Thrust and Neogene crustal exhumation in the Bhutanese Himalaya derived from
636 inversion of multithermochronologic data, Journal of Geophysical Research-Solid Earth,
637 119(2), 1446-1481, doi:10.1002/2013jb010891.

638 Currie, B.S., P.J. Polissar, D.BRowley, M. Ingalls, S. Li, G. Olack, and K.H. Freeman (2016),
639 Multiproxy paleoaltimetry of the late Oligocene-Pliocene Oiyug basin, southern Tibet,
640 American Journal of Science, 316, 401-436.

DeCelles, P. G., I. S. Castaneda, B. Carrapa, J. Liu, J. Quade, R. Leary, and L. Zhang (2018), Oligocene-Miocene Great Lakes in the India-Asia Collision Zone, Basin Research, 30, 228-247, doi:10.1111/bre.12217.

DeCelles, P.G., P. Kapp, G.E. Gehrels, and L. Ding (2014), Paleocene-Eocene foreland basin evolution in the Himalaya of southern Tibet and Nepal: Implications for the age of initial India-Asia collision, Tectonics, 33, 824–849, doi:10.1002/2014TC003522.

DeCelles, P. G., P. Kapp, J. Quade, and G. E. Gehrels (2011), Oligocene-Miocene Kailas basin, southwestern Tibet: Record of postcollisional upper-plate extension in the Indus-Yarlung suture zone, Geological Society of America Bulletin, 123(7-8), 1337-1362, doi:10.1130/b30258.1.

DeCelles, P.G., G.E. Gehrels, Y. Najman, A.J., Martin, A. Carter, and E. Garzanti (2004), Detrital geochronology and geochemistry of Cretaceous–Early Miocene strata of Nepal: implications for timing and diachroneity of initial Himalayan orogenesis, Earth and Planetary Science Letters, 227, 313-330, doi:10.1016/j.epsl.2004.08.019.

Dewey, J.F. (1988), Extensional collapse of orogens, Tectonics, 7(6), 1123-1139.

Ding, L., Q. Xu, Y. Yue, H. Wang, F. Cai, and S. Li (2014), The Andean-type Gangdese Mountains: Paleo elevation record from the Paleocene–Eocene Linzhou Basin, Earth and Planetary Science Letters, 392, 250-264.

Donelick, R.A., and D.S. Miller (1991), Enhanced TINT fission-track densities in low spontaneous track density apatites using cf-252-derived fission fragment tracks - a model and experimental-observations. Nuclear Tracks and Radiation Measurements, 18, 301-307.

Donelick, R.A., P.B. O'Sullivan, and R.A. Ketcham (1999), Apatite fission-track analysis. Reviews in Mineralogy & Geochemistry, 58, 49-94.

Gallagher, K. (2012), Transdimensional inverse thermal history modeling for quantitative thermochronology, Journal of Geophysical Research-Solid Earth, 117, doi:10.1029/2011jb008825.

Ge, Y., J. Dai, C. Wang, Y. Li, G. Xu, and M. Danisik (2017), Cenozoic thermo-tectonic evolution of the Gangdese batholith constrained by low-temperature thermochronology, Gondwana Research, 41, 451-462.

Ge Y., Y. Li, X. Wang, X. Qian, J. Zhang, A. Zhou, and J. Liu-Zeng (2018), Oligocene-Miocene burial and exhumation of the southernmost Gangdese mountains from sedimentary and thermochronological evidence, Tectonophysics, 723, 68-80.

Gourbet, L., G. Maheo, P. H. Leloup, J.-L. Paquette, P. Sorrel, M. Henriquet, X. Liu, and X. Liu (2017), Western Tibet relief evolution since the Oligo-Miocene, Gondwana Research, 41, 425-437, doi:10.1016/j.gr.2014.12.003.

Goussin, F., Riel, N., Cordier, C., Guillot, S., Boulvais, P., Roperch, P., Replumaz, A., Schulmann, K., Dupont-Nivet, G., Rosas, F., and Guo, Z. (2020), Carbonated inheritance in the Eastern Tibetan lithospheric mantle: Petrological evidences and geodynamic implications. Geochemistry, Geophysics, Geosystems, 21, e2019GC008495.

Guillaume, B., J. Martinod, L. Husson, M. Roddaz, and R. Riquelme (2009), Neogene uplift of central eastern Patagonia: Dynamic response to active spreading ridge subduction?, Tectonics, 28, doi:10.1029/2008tc002324.

Guillot, S., E. Garzanti, D. Baratoux, D. Marquer, G. Maheo, and J. de Sigoyer (2003), Reconstructing the total shortening history of the NW Himalaya, Geochemistry Geophysics Geosystems, 4(7), 1064, doi:10.1029/2002GC000484.

Gurnis, M., and S. Zhong (1991), Generation of long wavelength heterogeneity in the mantle by the dynamic interaction between plates and convection, Geophysical Research Letters, 18(4), 581-584, doi:10.1029/91gl00823.

Harper, J. F. (1984), Mantle flow due to internal vertical forces, Physics of the Earth and Planetary Interiors, 36, 285-290, doi:10.1016/0031-9201(84)90052-9.

Harrison, T. M., P. Copeland, W. S. F. Kidd, and A. Yin (1992), Raising Tibet, Science, 255(5052), 1663-1670, doi:10.1126/science.255.5052.1663.

Harrison, T. M., A. Yin, M. Grove, O. M. Lovera, F. J. Ryerson, and X. H. Zhou (2000), The Zedong Window: A record of superposed Tertiary convergence in southeastern Tibet, Journal of Geophysical Research-Solid Earth, 105(B8), 19211-19230, doi:10.1029/2000jb900078.

Harrison, T.M., E.B. Watson, and A.B. Aikman (2007), Temperature spectra of zircon crystallization in plutonic rocks, Geology, 35(7), 635-638.

Hu, X., E. Garzanti, J. Wang, W. Huang, W. An, and A. Webb (2016), The timing of India-Asia collision onset – Facts, theories, controversies, Earth-Science Reviews, 160, 264-299, doi:10.1016/j.earscirev.2016.07.014.

Heim, A., and A. Gansser (1939), Central Himalayan geological observations of the Swiss expedition, Mem. Sos. Halv. Nat, 77(1), 245.

Horton, B.K., A. Yin, M.S. Spurlin, J. Zhou, and J. Wang (2002), Paleocene–Eocene syncontractional sedimentation in narrow, lacustrine-dominated basins of east-central Tibet, Geological Society of America Bulletin, 114(7), 771-186, dio:10.1130/0016-7606(2002)114<0771:PESSIN>2.0.CO;2

Hurford, A.J., and P.F. Green (1982), A users' guide to fission track dating calibration. Earth Planet. Sci. Lett., 59, 343-354.

Husson, L. (2006), Dynamic topography above retreating subduction zones, Geology, 34(9), 741-744, doi:10.1130/g22436.1.

Husson, L., M. Bernet, S. Guillot, P. Huyghe, J.-L. Mugnier, A. Replumaz, X. Robert, and P. Van der Beek (2014), Dynamic ups and downs of the Himalaya, Geology, 42(10), 839-842, doi:10.1130/g36049.1.

Husson, L., B. Guillaume, F. Funiciello, C. Faccenna, and L. H. Royden (2012), Unraveling topography around subduction zones from laboratory models, Tectonophysics, 526, 5-15, doi:10.1016/j.tecto.2011.09.001.

719 Jackson, S.E., N.J. Pearson, W.L. Griffin, and E.A. Belousova (2004), The application of laser
720 ablation-inductively coupled plasma-mass spectrometry to in situ U-Pb zircon
721 geochronology. Chemical Geology, 211, 47-69.

722 Kapp, P., and P.G. DeCelles (2019), Mesozoic–Cenozoic geological evolution of the Himalayan-
723 Tibetan orogen and working tectonic hypotheses, American Journal of Science, 319(3),
724 159-254.

725 Kapp, P., M. A. Murphy, A. Yin, T. M. Harrison, L. Ding, and J. H. Guo (2003), Mesozoic and
726 Cenozoic tectonic evolution of the Shiquanhe area of western Tibet, Tectonics, 22(4),
727 doi:10.1029/2001tc001332.

728 Kapp, P., P.G. DeCelles, A.L. Leier, J.M. Fabijanic, S. He, A. Pullen, and G.E. Gehrels (2007),
729 The Gangdese retroarc thrust belt revealed, Geological Society of America Today, 17(7),
730 4-9, doi: 10.1130/GSAT01707A.1.

731 Ketcham, R.A., R.A. Donelick, and W. Carlson (1999), Variability of apatite fission-track
732 annealing kinetics: III. Extrapolation to geological time scales. American Mineralogist,
733 84, 1235-1255.

734 Ketcham, R. A., A. Carter, R. A. Donelick, J. Barbarand, and A. J. Hurford (2007), Improved
735 measurement of fission-track annealing in apatite using c-axis projection, American
736 Mineralogist, 92(5-6), 789-798, doi:10.2138/am.2007.2280.

737 Kirstein, L. A., H. Sinclair, F. M. Stuart, and K. Dobson (2006), Rapid early Miocene
738 exhumation of the Ladakh batholith, western Himalaya, Geology, 34(12), 1049-1052,
739 doi:10.1130/g22857a.1.

740 Kohn, M. J., E. J. Catlos, F. J. Ryerson, and T. M. Harrison (2001), Pressure-temperature-time
741 path discontinuity in the Main Central thrust zone, central Nepal, Geology, 29(7), 571-
742 574, doi:10.1130/0091-7613(2001)029<0571:pttpdi>2.0.co;2.

743 Lacassin, R., et al. (2004), Large-scale geometry, offset and kinematic evolution of the
744 Karakorum fault, Tibet, Earth and Planetary Science Letters, 219(3-4), 255-269,
745 doi:10.1016/s0012-821x(04)00006-8.

746 Laskowski, A. K., P. Kapp, and F. Cai (2018), Gangdese culmination model: Oligocene-Miocene
747 duplexing along the India-Asia suture zone, Lazi region, southern Tibet, Geological
748 Society of America Bulletin, 130(7-8), 1355-1376, doi:10.1130/b31834.1.

749 Laskowski, A. K., P. Kapp, L. Ding, C. Campbell, and X. Liu (2017), Tectonic evolution of the
750 Yarlung suture zone, Lopu Range region, southern Tibet, Tectonics, 36(1), 108-136,
751 doi:10.1002/2016tc004334.

752 Leary, R., D. A. Orme, A. K. Laskowski, P. G. DeCelles, P. Kapp, B. Carrapa, and M. Dettinger
753 (2016a), Along-strike diachroneity in deposition of the Kailas Formation in central
754 southern Tibet: Implications for Indian slab dynamics, Geosphere, 12(4), 1198-1223,
755 doi:10.1130/ges01325.1.

756 Leary, R., P.G. DeCelles, J. Quade, G.E. Gehrels and G. Waanders (2016b), The Liuqu
757 Conglomerate, southern Tibet: Early Miocene basin development related to deformation
758 within the Great Counter Thrust system, Lithosphere, 8(5), 427-450.

759 Li, G., Y. Tian, B. P. Kohn, M. Sandiford, Z. Xu, and Z. Cai (2015a), Cenozoic low temperature
760 cooling history of the Northern Tethyan Himalaya in Zedang, SE Tibet and its
761 implications, Tectonophysics, 643, 80-93, doi:10.1016/j.tecto.2014.12.014.

762 Li, G., B. Kohn, M. Sandiford, Z. Xu, and L. Wei (2015b), Constraining the age of Liuqu
763 Conglomerate, southern Tibet: Implications for evolution of the India–Asia collision
764 zone, Earth and Planetary Science Letters, 426, 259-266.

765 Li, G., B. Kohn, M. Sandiford, and Z. Xu (2017), India-Asia convergence: Insights from burial
766 and exhumation of the Xigaze fore-arc basin, south Tibet, Journal of Geophysical
767 Research: Solid Earth, 122, 3430-3449.

768 Liu, Y., Z. Hu, S. Gao, D. Guenther, J. Xu, C. Gao, and H. Chen (2008), In situ analysis of major
769 and trace elements of anhydrous minerals by LA-ICP-MS without applying an internal
770 standard. Chemical Geology, 257, 34-43.

771 Liu, Y.S., S. Gao, Z. Hu, C. Gao, K. Zong, and D. Wang (2010), Continental and oceanic crust
772 recycling-induced melt-peridotite interactions in the Trans-North China Orogen: U-Pb
773 dating, Hf isotopes and trace elements in zircons of mantle xenoliths. Journal of
774 Petrology, 51, 537–571.

775 Ludwig, K. (2012), User's manual for Isoplot 3.75. A geological toolkit for Microsoft Excel, in
776 Berkeley Geochronology Center Special Publication No. 5, edited.

777 Lyon-Caen, H., and P. Molnar (1983), Constraints on the structure of the Himalaya from an
778 analysis of gravity-anomalies and a flexural model of the lithosphere, Journal of
779 Geophysical Research, 88(NB10), 8171-8191, doi:10.1029/JB088iB10p08171.

780 Mahéo, G., J. Blichert-Toft, C. Pin, S. Guillot, and A. Pecher (2009), Partial Melting of Mantle
781 and Crustal Sources beneath South Karakorum, Pakistan: Implications for the Miocene
782 Geodynamic Evolution of the IndiaAsia Convergence Zone, Journal of Petrology, 50(3),
783 427-449, doi:10.1093/petrology/egp006.

784 Mahéo, G., S. Guillot, J. Blichert-Toft, Y. Rolland, and A. Pecher (2002), A slab breakoff model
785 for the Neogene thermal evolution of South Karakorum and South Tibet, Earth and
786 Planetary Science Letters, 195(1-2), 45-58, doi:10.1016/s0012-821x(01)00578-7.

787 Miller, C., R. Schuster, U. Klotzli, W. Frank, and F. Purtscheller (1999), Post-collisional potassic
788 and ultrapotassic magmatism in SW Tibet: Geochemical and Sr-Nd-Pb-O isotopic
789 constraints for mantle source characteristics and petrogenesis, Journal of Petrology,
790 40(9), 1399-1424, doi:10.1093/petrology/40.9.1399.

791 Mo, X., Y. Niu, G. Dong, Z. Zhao, Z. Hou, S. Zhou, and S. Ke (2008), Contribution of
792 syncollisional felsic magmatism to continental crust growth: A case study of the
793 Paleogene Linzizong volcanic Succession in southern Tibet, Chemical Geology, 250(1-
794 4), 49-67, doi:10.1016/j.chemgeo.2008.02.003.

795 Molnar, P., P. England, and J. Martinod (1993), Mantle dynamics, uplift of the Tibetan Plateau,
796 and the Indian monsoon, Reviews of Geophysics, 31(4), 357-396,
797 doi:10.1029/93rg02030.

798 Morgan, W. J. (1965), Gravity anomalies and convection currents: 1. A sphere and cylinder
799 sinking beneath the surface of a viscous fluid, Journal of Geophysical Research, 70(24),
800 6175-6187.

801 Murphy, M. A., and A. Yin (2003), Structural evolution and sequence of thrusting in the Tethyan
802 fold-thrust belt and Indus-Yalu suture zone, southwest Tibet, Geological Society of
803 America Bulletin, 115(1), 21-34, doi:10.1130/0016-
804 7606(2003)115<0021:seasot>2.0.co;2.

805 Najman, Y., A. Carter, G. Oliver, and E. Garzanti (2005), Provenance of Eocene foreland basin
806 sediments, Nepal: Constraints to the timing and diachroneity of early Himalayan
807 orogenesis, Geology, 33(4), 309-312, doi: 10.1130/G21161.1.

808 Najman, Y., E. Appel, M. Boudagher-Fadel, P. Bown, A. Carter, E. Garzanti, L. Godin, J. Han,
809 U, Liebke, G, Oliver, R. Parrish, and G. Vezzoli (2010), Timing of India-Asia collision:
810 Geological, biostratigraphic, and palaeomagnetic constraints, Journal of Geophysical
811 Research, 115, B12416, doi:10.1029/2010JB007673.

812 Najman, Y., S. D. Burley, A. Copley, M. J. Kelly, K. Pander, and P. Mishra (2018), The Late
813 Eocene-Early Miocene Unconformities of the NW Indian Intraplate Basins and
814 Himalayan Foreland: A Record of Tectonics or Mantle Dynamics?, Tectonics, 37(10),
815 3970-3985, doi:10.1029/2018tc005286.

816 Ning, Z., L. Zhang, K.W. Huntington, C. Wang, J. Dai, Z. Han, B.H. Passey, X. Qian, and J.
817 Zhang (2019), The burial and exhumation history of the Liuqu Conglomerate in the
818 Yarlung Zangbo suture zone, southern Tibet: Insights from clumped isotope
819 thermometry, Journal of Asian Earth Sciences, 174, 205-217.

820 Pan, Y., P. Copeland, M.K. Roden, W.S.F. Kidd, and T.M. Harrison (1993), Thermal and
821 unroofing history of the Lhasa area, southern Tibet – evidence from apatite fission track
822 thermochronology, Nucl. Tracks Radiat. Meas., 21, 543-554.

823 Pitard, P., A. Replumaz, F. Funiciello, L. Husson, and C. Faccenna (2018), Mantle kinematics
824 driving collisional subduction: Insights from analogue modeling, Earth and Planetary
825 Science Letters, 502, 96-103.

826 Pullen, A., P. Kapp, P. G. DeCelles, G. E. Gehrels, and L. Ding (2011), Cenozoic anatexis and
827 exhumation of Tethyan Sequence rocks in the Xiao Curia Range, Southwest Tibet,
828 Tectonophysics, 501(1-4), 28-40, doi:10.1016/j.tecto.2011.01.008.

829 Ratschbacher, L., W. Frisch, G. Liu, and C.C. Chen (1994), Distributed deformation in southern
830 and western Tibet during and after the India-Asian collision, Journal of Geophysical
831 Research, 99, 19917–19945, doi:10.1029/94JB0093.

832 Replumaz, A., and P. Tapponnier (2003), Reconstruction of the deformed collision zone between
833 India and Asia by backward motion of lithospheric blocks, Journal of Geophysical
834 Research: Solid Earth, 108(B6).

835 Replumaz, A., A. M. Negredo, A. Villasenor, and S. Guillot (2010), Indian continental
836 subduction and slab break-off during Tertiary collision, Terra Nova, 22(4), 290-296,
837 doi:10.1111/j.1365-3121.2010.00945.x.

838 Replumaz, A., F.A. Capitanio, S. Guillot, A.M. Negredo, and A. Villaseñor (2014), The coupling
839 of Indian subduction and Asian continental tectonics, Gondwana Research, 26(2), 608-
840 626, doi:10.1016/j.gr.2014.04.003.

841 Replumaz, A., F. Funiciello, R. Reitano, C. Faccenna, and M. Balon (2016), Asian collisional
842 subduction: A key process driving formation of the Tibetan Plateau, Geology, 44911),
843 943-946, doi:10.1130/G38276.1.

844 Rex, A. J., M. P. Searle, R. Tirrul, M. B. Crawford, D. J. Prior, D. C. Rex, and A. Barnicoat
845 (1988), The geochemical and tectonic evolution of the Central Karakoram, North
846 Pakistan, Philosophical Transactions of the Royal Society a-Mathematical Physical and
847 Engineering Sciences, 326(1589), 229-255, doi:10.1098/rsta.1988.0086.

848 Ricard, Y., M. Richards, C. Lithgowbertelloni, and Y. Lestunff (1993), A geodynamic model of
849 mantle density heterogeneity, Journal of Geophysical Research-Solid Earth, 98(B12),
850 21895-21909, doi:10.1029/93jb02216.

851 Rohrmann, A., P. Kapp, B. Carrapa, P. W. Reiners, J. Guynn, L. Ding, and M. Heizler (2012),
852 Thermochronologic evidence for plateau formation in central Tibet by 45 Ma, Geology,
853 40(2), 187-190, doi:10.1130/g32530.1.

854 Sanchez, V. I., M. A. Murphy, A. C. Robinson, T. J. Lapen, and M. T. Heizler (2013), Tectonic
855 evolution of the India-Asia suture zone since Middle Eocene time, Lopukangri area,
856 south-central Tibet, Journal of Asian Earth Sciences, 62, 205-220,
857 doi:10.1016/j.jseaes.2012.09.004.

858 Shen, T., G. Wang, P. H. Leloup, P. van der Beek, M. Bernet, K. Cao, A. Wang, C. Liu, and K.
859 Zhang (2016), Controls on Cenozoic exhumation of the Tethyan Himalaya from fission-
860 track thermochronology and detrital zircon U-Pb geochronology in the Gyirong basin
861 area, southern Tibet, Tectonics, 35(7), 1713-1734, doi:10.1002/2016tc004149.

862 Shen, T., G. Wang, M. Bernet, A. Replumaze, A. Ke, B. Song, K. Zhang, and P. Zhang (2019),
863 Long-term exhumation history of the Gangdese magmatic arc: Implications for the
864 evolution of the Kailas Basin, western Tibet, Geological Journal, doi: 10.1002/gj.3539.

865 Spicer, R. A., N. B. W. Harris, M. Widdowson, A. B. Herman, S. X. Guo, P. J. Valdes, J. A.
866 Wolfe, and S. P. Kelley (2003), Constant elevation of southern Tibet over the past 15
867 million years, Nature, 421(6923), 622-624, doi:10.1038/nature01356.

868 Spurlin, M.S.; A. Yin, B.K. Horton, J. Zhou, and J. Wang (2005), Structural evolution of the
869 Yushu-Nangqian region and its relationship to syncollisional igneous activity east-central
870 Tibet, Geological Society of America Bulletin, 177(9-10), 1293-1317,
871 doi:10.1130/B25572.1.

872 Tapponnier, P., Z. Xu, F. Roger, B. Meyer, N. Araund, G. Wittlinger and J. Yang (2001),
873 Oblique Stepwise Rise and Growth of the Tibet Plateau, Science, 294, 1671-1677, doi:
874 10.1126/science.105978.

875 Tremblay, M. M., M. Fox, J. L. Schmidt, A. Tripathy-Lang, M. M. Wielicki, T. M. Harrison, P.
876 K. Zeitler, and D. L. Shuster (2015), Erosion in southern Tibet shut down at similar to 10
877 Ma due to enhanced rock uplift within the Himalaya, Proceedings of the National
878 Academy of Sciences of the United States of America, 112(39), 12030-12035,
879 doi:10.1073/pnas.1515652112.

880 Valley, J.W., A.J. Cavosie, B. Fu, W.H. Peck, and S.A. Wilde (2006), Comment on
881 "Heterogeneous Hadean hafnium: Evidence of continental crust at 4.4 to 4.5 Ga",
882 Science, 312, 1139a, doi: 10.1126/science.1125301.

883 Valli, F., N. Arnaud, P. H. Leloup, E. R. Sobel, G. Maheo, R. Lacassin, S. Guillot, H. Li, P.
884 Tapponnier, and Z. Xu (2007), Twenty million years of continuous deformation along the
885 Karakorum fault, western Tibet: A thermochronological analysis, Tectonics, 26(4),
886 doi:10.1029/2005tc001913.

887 Van der Voo, R., W. Spakman, and H. Bijwaard (1999), Tethyan subducted slabs under India,
888 Earth and Planetary Science Letters, 171(1), 7-20, doi:10.1016/s0012-821x(99)00131-4.

889 Vermeesch, P. (2009), RadialPlotter: A Java application for fission track, luminescence and other
890 radial plots. Radiat. Measur., 44, 409–410.

891 Wang, Y., X. Zhang, L. Sun and J. Wan (2007), Cooling history and tectonic exhumation stages
892 of the south-central Tibetan Plateau (China): constrained by $^{40}Ar/^{39}Ar$ and apatite fission
893 track thermochronology, Journal of Asian Earth Sciences, 29, 266-282.

894 Wang, E., P. J. J. Kamp, G. Xu, K. V. Hodges, K. Meng, L. Chen, G. Wang, and H. Luo (2015),
895 Flexural bending of southern Tibet in a retro foreland setting, Scientific Reports, 5,
896 doi:10.1038/srep12076.

897 Wang, G., K. Zhang, S. Xiang, A. Wang, and K. Cao (2014), Cenozoic geological map of the
898 Tibetan Plateau and adjacent areas, Press of China University of Geosciences, Wuhan.

899 Webb, A. A. G., H. Guo, P. D. Clift, L. Husson, T. Mueller, D. Costantino, A. Yin, Z. Xu, H.
900 Cao, and Q. Wang (2017), The Himalaya in 3D: Slab dynamics controlled mountain
901 building and monsoon intensification, Lithosphere, 9(4), 637-651, doi:10.1130/l636.1.

902 Williams, H. M., S. P. Turner, J. A. Pearce, S. P. Kelley, and N. B. W. Harris (2004), Nature of
903 the source regions for post-collisional, potassic magmatism in southern and northern
904 Tibet from geochemical variations and inverse trace element modelling, Journal of
905 Petrology, 45(3), 555-607, doi:10.1093/petrology/egg094.

906 Wu, Y. (1979), Tertiary of the Tibet, Tibetan Bureau of Geology and Mineral Resources.

907 Yamada, R., M. Murakami, and T. Tagami (2007), Statistical modelling of annealing kinetics of
908 fission tracks in zircon; Reassessment of laboratory experiments, Chemical Geology,
909 236(1-2), 75-91, doi:10.1016/j.chemgeo.2006.09.002.

910 Yang, T.F., J.R. Wang, C.H. Lo, S.L. Chung, R.L. Tien, R. Xu, and W. Deng (1999), The
911 thermal history of the Lhasa block, south Tibetan Plateau based on FTD and Ar-Ar
912 dating, Radiation Measurements, 31, 627-632.

913 Yang, M., F. E. Nelson, N. I. Shiklomanov, D. Guo, and G. Wan (2010), Permafrost degradation
914 and its environmental effects on the Tibetan Plateau: A review of recent research, Earth-
915 Science Reviews, 103(1-2), 31-44, doi:10.1016/j.earscirev.2010.07.002.

916 Yin, A. (2010), Cenozoic tectonic evolution of Asia: A preliminary synthesis, Tectonophysics,
917 488(1-4), 293-325.

918 Yin, A., and T.H. Harrison (2000), Geologic evolution of the Himalayan-Tibetan orogen, Annu.
919 Rev. Earth Planet. Sci., 28, 211–80.

Yin, A. (2000), Mode of Cenozoic east-west extension in Tibet suggesting a common origin of rifts in Asia during the Indo-Asian collision, Journal of Geophysical Research-Solid Earth, 105(B9), 21745-21759, doi:10.1029/2000jb900168.

Yin, A., T. M. Harrison, M. A. Murphy, M. Grove, S. Nie, F. J. Ryerson, W. X. Feng, and C. Z. Le (1999), Tertiary deformation history of southeastern and southwestern Tibet during the Indo-Asian collision, Geological Society of America Bulletin, 111(11), 1644-1664, doi:10.1130/0016-7606(1999)111<1644:tdhosa>2.3.co;2.

Yin, A., T.M. Harrison, F.J. Ryerson, C. Wenji, W.S.F. Kidd, and P. Copeland (1994), Tertiary structural evolution of the Gangdese thrust system, southeastern Tibet, Journal of Geophysical research, 99 (B9), 18175-18201.

Zhang, K., G. Wang, M. Luo, Y. Xu, B. Song, and J. Ji (2014), Palaeogene–Neogene stratigraphic sequences of the Tibetan Plateau and their response to plateau uplift, In R. Rocha et al. (eds.), STRATI 2013, Springer Geology, doi: 10.1007/978-3-319-04364-7_122.

Zhang, L., M. N. Ducea, L. Ding, A. Pullen, P. Kapp, and D. Hoffman (2014), Southern Tibetan Oligocene-Miocene adakites: A record of Indian slab tearing, Lithos, 210, 209-223, doi:10.1016/j.lithos.2014.09.029.

Zhao, Z., T. Li, J. Luo, and H. Lu (2011), Stratigraphy of the Tibetan Plateau, Science Press, Beijing.

Zhao, B., Huang, Y., Zhang, C., Wang, W., Tan, K., Du, R. (2015). Crustal deformation on the Chinese mainland during 1998–2014 based on GPS data. Geodesy Geodyn.6, 7–15, doi:10.1016/j.geog.2014.12.006.

Zhao, J., K. Qi, G. Li, M. Cao, N.J. Evans, B.I.A. McInnes, J. Li, B. Xiao, and L. Chen (2015), The exhumation history of collision-related mineralizing systems in Tibet: Insights from thermal studies of the Sharang and Yaguila deposits, central Lhasa, Ore Geology Reviews, 65, 1043-1061.

Zhu, D., Z. Zhao, Y. Niu, X. Mo, S. Chung, Z. Hou, L. Wang, and F. Wu (2011), The Lhasa Terrane: Record of a microcontinent and its histories of drift and growth, Earth and Planetary Science Letters, 301, 241-255.

Zhu, Y., X. Fang, J. Gao, H. Yi, S. Wang, and W. Zhang (2006), Oligo-Mioence depositional facies of the Wuyu basin, southern Tibetan Plateau, Acta Sedimentologica Sinica, 24, 775–782.

952 **Figure 1.** Schematic structural framework of southern Tibet and the Himalaya. Age data of
953 magmatism are from the *Tibetan Magmatism Database* (https://www.jaychapman.org/tibet-
954 magmatism-database.html) by *Chapman & Kapp* [2017], with contours from *Goussin et al.*
955 [2020]. Thermochronological data are cited from 1) *Kirstein et al.* [2006]; 2) *Carrapa et al.*
956 [2014]; 3) *Tremblay et al.* [2015]; 4) *Li et al.* [2015a]; 5) *Li et al.* [2015b]; 6) *Shen et al.* [2016].
957 The yellow box indicates the location of Figure 2, and the green box indicates the location of
958 Figure 5. JRS: Jinsha suture; BNS: Banggong-Nujiang suture; IYS: Indus-Yarlung suture; GCT:
959 Great Counter Thrust; KF: Kunlun Fault; KKF: Karakorum Fault; STF: South Tibetan Fault;
960 MCT: Main Central Thrust; MBT: Main Boundary Thrust; MFT: Main Front Thrust; GM: Gurla
961 Mandhata.

962 **Figure 2.** Detailed geological map of the Mt. Kailas area, showing the sample locations and
963 previous thermochronological data in study area: grey, *Yin et al.* [1999]); violet, *DeCelles et al.*
964 [2011]; yellow, *Pullen et al.* [2011]; cyan, *Carrapa et al.* [2014]. Cross-sections with sample
965 locations are shown below the map.

966 **Figure 3.** U-Pb concordia diagrams of sample 13T02 (top) and 14T05 (bottom) using the
967 program Isoplot [*Ludwig*, 2012]. The data reduction procedures are described in *Liu et al.* [2008,
968 2010] with GJ-1 zircon standards [*Jackson et al.*, 2004].

969 **Figure 4.** A. Age-elevation plots for dated samples and selected previous $^{40}Ar/^{39}Ar$ datum [*Yin et*
970 *al.*, 1999]. Samples with red labels are used for QTQt modeling. B. QTQt model results taking
971 samples 13T01, 13T02 and 13T04 as a profile. The red line corresponds to the path of the hottest
972 (lowest elevation) sample (with the 95% credible interval range in magenta); the blue line
973 corresponds to the coolest (highest elevation) sample (with the 95% credible interval range in
974 cyan); intermediate samples are shown in grey. C. The predicted data by the QTQt modeling
975 compared with observed data. The red box is the general prior time-temperature box, which was
976 set to a temperature of 200 ± 200 °C [*Ketcham et al.*, 2007], and the black boxes are geological
977 constraints on the modeling (see the text and Table 1 for details).

978 **Figure 5.** Drainage network related to the modern river sand sample (red star). Main lithologic
979 units of the northern Gangdese magmatic arc are shown in the figure. Inset figure illustrates the
980 RadialPlotter plot of the ZFT data from the modern river sand.

981 **Figure 6.** Simplified geodynamic evolution of Indian subduction, the Himalaya and southern
982 Tibet. Green curves above cross-sections (left) and map views (right) of the modeled dynamic
983 surface uplift and subsidence (differences in dynamic topography over the time frames) for an
984 idealized Indian-Eurasian subduction zone, with dynamic surface uplift (air compensated),
985 dynamic subsidence (sediment compensated), or equivalent erosion (assuming steady elevation).
986 Slab geometries at each time are based on geophysical observations for present-day, and
987 geological arguments for past reconstructions in the past complemented by lessons from
988 numerical and analogue models (left). The black line is the zero isocontour, representing 0
989 uplift/subsidence

990 **Figure 7.** Schematic diagrams showing the dynamic deflection/uplift of southern Tibet.(A and
991 B) Between 26 and 21 Ma, the southward migration of the dynamic deflection resulted in the
992 uplift of the northern part of the Gangdese magmatic arc and subsidence of southernmost Tibet,

forming the Kailas basin. (C and D) Beginning at approximately 20 Ma, surface uplift took place in southernmost Tibet, and subsidence migrated toward the front of the Himalaya, resulting in rapid exhumation of the Kailas Formation and Gangdese batholith. The figures D and E zoom in the topographic evolution around the Kailas basin during 26-21 and 20-15 Ma. The green curve on the top shows the dynamic subsidence (sediment compensated) as in the Fig. 6.

Figure 8. Compilation of the existing thermochronologic data in southern Tibet with the present-day dynamic deflection [*Husson et al.*, 2014]. (A) Distribution of the AFT and AHe data of the Kailas Formation, Gangdese batholith and Xigaze basin with the model-predicted dynamic surface uplift (red) and subsidence (blue) at present day as well as the depth contours of the foreland basin (yellow) [*Husson et al.*, 2014]. The contour values (km) are for a sediment compensation of dynamic subsidence (blue) or erosion compensated dynamic surface uplift (red). In the absence of erosion or surface uplift, the magnitude should be divided by a factor of ~6 (see *Husson et al.* [2014] for details). The age of magmatism contours by *Goussin et al.* [2020] are also illustrated. (B-D) AFT, AHe and ZHe ages of the Kailas Formation, Gangdese batholith and Xigaze basin against the distance from Indus-Yarlung suture zone in different locations. The data are summarized from *Pan et al.* [1993], *Copeland et al.* [1995], *Yang et al.* [1999], *Wang et al.* [2007], *Dai et al.* [2013], *Carrapa et al.* [2014], *Wang et al.* [2015], *Li et al.* [2015a, 2015b, 2016, 2017], *Tremblay et al.* [2015], J. *Zhao et al.* [2015], *Ge et al.* [2017, 2018], and this study.

Table 1. Thermal history input table for the QTQt modeling

Table 2. Bedrock ZFT results from the Gangdese batholith

Table 3. Bedrock AFT results from the Gangdese batholith

Table 4. Detrital zircon fission-track data from sample T44-1

Table 1

1. Thermochronologic Data

Samples and data used in modeling

Sample	AFT ages	AFT lengths	ZFT ages
13T01	x	x	x
13T02	x	x	x
13T04	x		x

Data treatment

The AFT lengths are measured from *cf tracks* and using *c-axis* projected lengths (Ketcham et al., 2007), with initial track length of 16.3 μm. The term for the kinetic parameter is *Dpar* [*Donelick et al.*, 1999; *Ketcham et al.*, 1999*]*.

The AFT ages and lengths are combined in one data set for an individual sample, while the ZFT ages were regarded as another data input file for the same sample, with the same GPS information but different annealing parameters.

These data were modeled as an age-elevation profile.

2. Additional geologic information

Assumption	***Explanation and data source***
At a surface temperature of 0 ± 10 °C by 0 Ma	Based on the annual mean surface temperature of the Tibetan Plateau for the years from 1961 to 2000 [*Yang et al.*, 2010]
At a near-surface level during 32-26 Ma, assuming a temperature of 200 ± 200 °C	The Gangdese batholith was exposed at the surface before deposition of the Kailas Formation [*DeCelles et al.*, 2011; *Carrapa et al.*, 2014]. Available $^{40}Ar/^{39}Ar$ ages of K-feldspar for the Gangdese batholith in the Mt. Kailas area, close to our profile (ca. 15 to the west), suggest that the rocks experienced cooling after 32 Ma [*Yin et al.*, 1999].
Modeling begins at temperatures of 750-850 °C at 41.0±1.1 Ma	According to the U-Pb dating of sample 13T02 in this study

3. System- and model-specific parameters

AFT annealing model: *Ketcham et al.* [2007]

ZFT annealing model: *Yamada et al.* [2007] long term

Modeling Code: QTQt version 5.5.0 for PC user

Inversion scheme: Bayesian transdimensional Markov chain Monte Carlo (MCMC)

Ranges for general prior:

Time (Myr): oldest observed age ± oldest observed age (i.e., 24.1 ± 24.1 here)

Temperature (°C): 200 ± 200

Maximum $\partial T/\partial t$ (°C/Myr): 1000

MCMC parameters:

Burn-in: 50,000 iterations; Post-burn-in: 200,000 iterations.

Table 2

No.	GPS	Elevation (m)	Lithology	ρ_s	N_s	ρ_i	N_i	ρ_d	N_d	N	$P(\chi^2)$	Dispersion	Pooled age (Ma)	U±2σ (ppm)
13T01	81.58389 31.08029	5447	Granite	8.11×10^6	1581	6.35×10^6	1239	2.54×10^5	3161	20	80.4%	1.2%	20.3±1.7	1253±78
13T02	81.58159 31.07923	5317	Granite	6.10×10^6	992	4.94×10^6	804	2.54×10^5	3161	20	65.7%	1.0%	19.6±2.0	974±73
13T04	81.53824 31.04565	5044	Granite	3.54×10^6	647	2.60×10^6	475	2.54×10^5	3161	19	97.6%	0.3%	21.7±2.7	513±49
14T01	82.05073 30.83476	5493	Diorite	5.43×10^6	1324	3.79×10^6	926	2.54×10^5	3161	20	98.4%	0.2%	22.7±2.1	748±53
14T03	82.02802 30.83046	5291	Diorite	2.78×10^6	550	1.83×10^6	362	2.54×10^5	3161	18	88.6%	0.6%	24.1±3.3	361±39
14T05	82.00145 30.82388	5104	Diorite	5.50×10^6	1197	4.08×10^6	887	2.54×10^5	3162	20	98.1%	0.4%	21.5±2.0	805±58

Note: All the samples were counted with a zeta calibration factor [*Hurford and Green*, 1982] $\xi = 125.66 \pm 1.86$ for glass dosimeter IRMM541. N = total number of grains counted; binomial peak-ages are given ± 2SE. The percentage of grains in a specific peak is also given. $P(\chi^2)$, χ^2 probability that the single grain ages represent one population.

Table 3

No.	ρ_s	N_s	ρ_i	N_i	ρ_d	N_d	N	$P(\chi^2)$	Dispersion	Pooled age (Ma)	U±2σ (ppm)	n	MTL (μm)	MTLc (μm)
13T01	3.50×10^5	403	2.83×10^6	3256	1.07×10^6	3394	20	98.0%	0.2%	16.3±1.9	40±2	135	12.70±1.83	13.89±1.32
13T02	2.31×10^5	275	2.24×10^6	2664	1.07×10^5	3405	20	91.9%	0.3%	13.7±1.8	31±2	77	12.60±1.87	13.74±1.38
13T04	9.77×10^4	84	1.08×10^6	926	1.07×10^6	3417	20	99.0%	0.1%	12.0±2.8	15±1			
14T01	1.31×10^5	162	1.18×10^6	1451	1.08×10^6	3428	24	75.7%	1.6%	14.9±2.5	16±1	41	13.13±1.57	14.22±1.09
14T03	1.46×10^5	72	1.51×10^6	745	1.08×10^6	3440	21	100.0%	0.1%	12.9±3.2	21±2			
14T05	1.43×10^5	141	1.67×10^6	1648	1.08×10^6	3451	30	99.9%	0.1%	11.5±2.1	23±1	37	13.76±1.54	14.59±1.14

Note: All the samples were counted with a zeta calibration factor $\xi = 247.47 \pm 6.05$ for glass dosimeter IRMM540R. N = total number of grains counted; binomial peak-ages are given ± 2SE. The percentage of grains in a specific peak is also given. $P(\chi^2)$, χ^2 probability that the single grain ages represent one population. n = number of horizontal confined track length measured; MTL, mean track length (with ± 1 Std. Dev., standard deviation). MTLc, mean track length of c-axis projected. All apatite samples for track length measurements were irradiated by a collimated beam of heavy ions released from a 252Cf source at the University of Melbourne (Australia) [*Donelick and Miller*, 1991].

1037 **Table 4**

Sample No.	GPS location	N	ρd×10^5cm^{-2} (N_d)	Ps×10^6cm^{-2} (N_s)	Pi×10^6cm^{-2} (N_i)	U (ug·g^{-1})	P(χ^2)	Dispersion	Age range (Ma)	P1 Age (Ma±1σ)	P2 Age (Ma±1σ)	P3 Age (Ma±1σ)	Central Age (Ma±1σ)
T44-1	81.08881 32.39525	100	3.837 (2686)	4.17 (3689)	3.02 (2669)	313	0	28%	15.0-96.0	27.3±1.3 (39.9±9.3%)	40.5±2.3 (50.7±8.6%)	70±8.1 (9±13%)	36.0±1.2

1038

Figure 1.

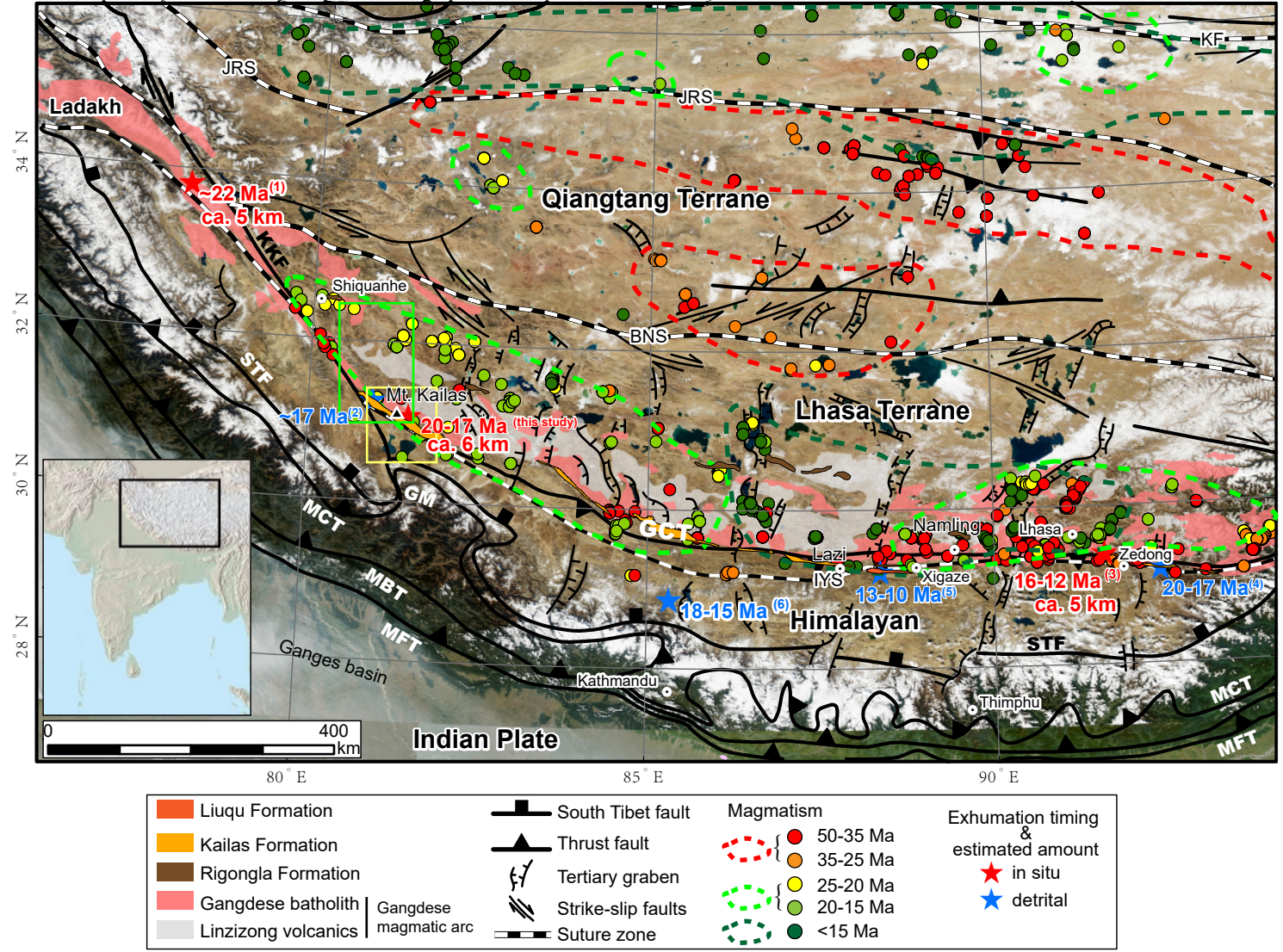
Ladakh
JRS
JRS
KF
~22 Ma (1)
ca. 5 km
KKF
Qiangtang Terrane
Shiquanhe
BNS
STF
Mt. Kailas
~17 Ma (2)
20-17 Ma (this study)
ca. 6 km
Lhasa Terrane
GM
MCT
GCT
Namling
Lhasa
Zedong
Lazi
IYS
Xigaze
13-10 Ma (5)
16-12 Ma (3)
ca. 5 km
20-17 Ma (4)
18-15 Ma (6)
Himalayan
MBT
MFT
Ganges basin
STF
Kathmandu
Thimphu
MCT
MFT
0
400
km
Indian Plate
34° N
32° N
30° N
28° N
80° E
85° E
90° E
Liuqu Formation
Kailas Formation
Rigongla Formation
Gangdese batholith
Linzizong volcanics
Gangdese magmatic arc
South Tibet fault
Thrust fault
Tertiary graben
Strike-slip faults
Suture zone
Magmatism
50-35 Ma
35-25 Ma
25-20 Ma
20-15 Ma
<15 Ma
Exhumation timing & estimated amount
in situ
detrital

Figure 2.

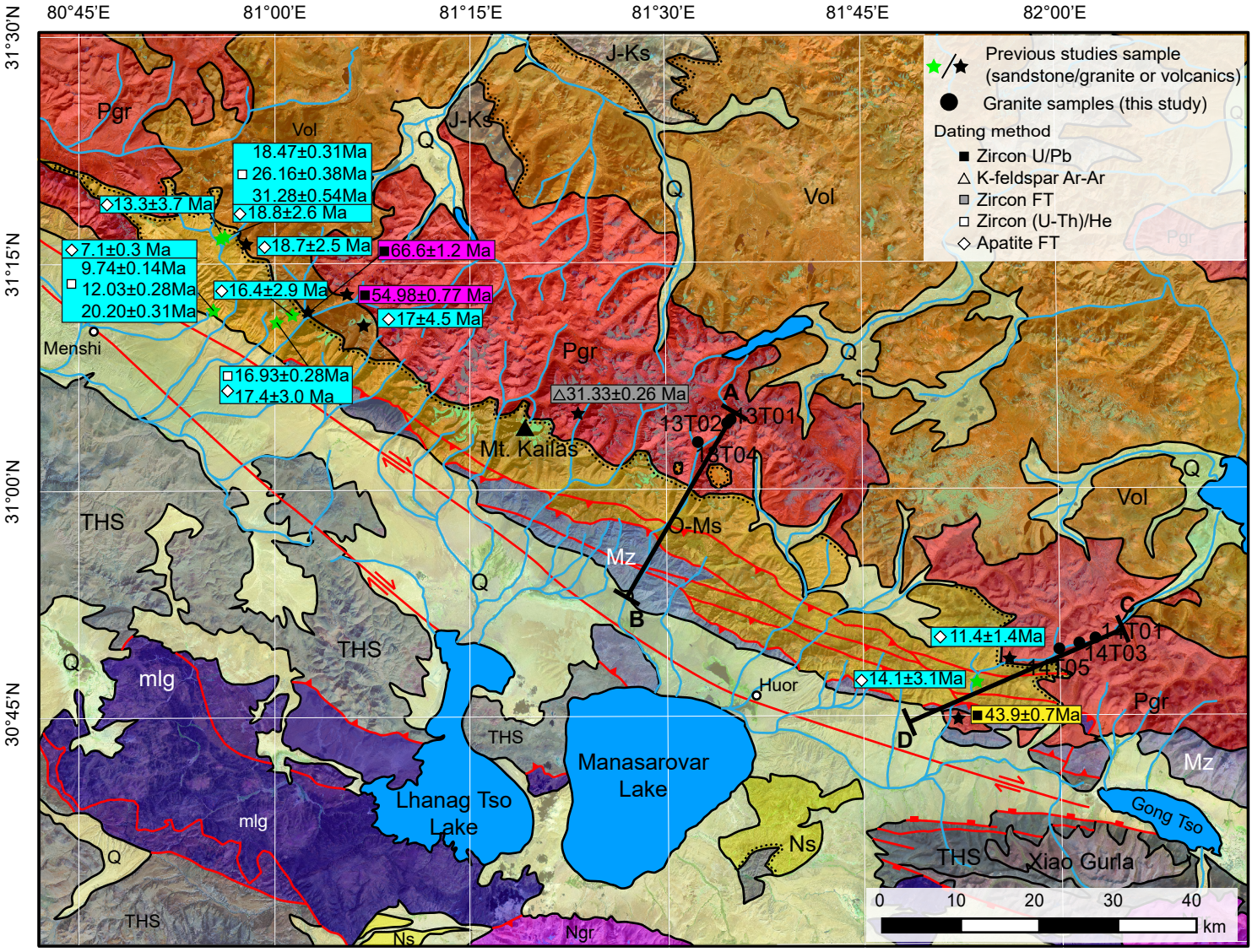

Q	Quaternary	Mz	Undifferential Mesozoic strata		Fault
Ns	Neogene sandstone	mlg	Mélange type rocks		Thrust Fault
O-Ms	Oligo-Miocene conglomerate (Kailas Formation)	THS	Tethyan Himalayan Sequence rocks		Low-angle normal fault
Vol	Volcanic rock (Linzizong Group)	Pgr	Paleogene granite (Gangdese granitoids)		Strike-slip fault
J-Ks	Jurassic-Cretaceous sandstone mudstone and limestone	Ngr	Miocene leucogranite		Sedimentary unconformity

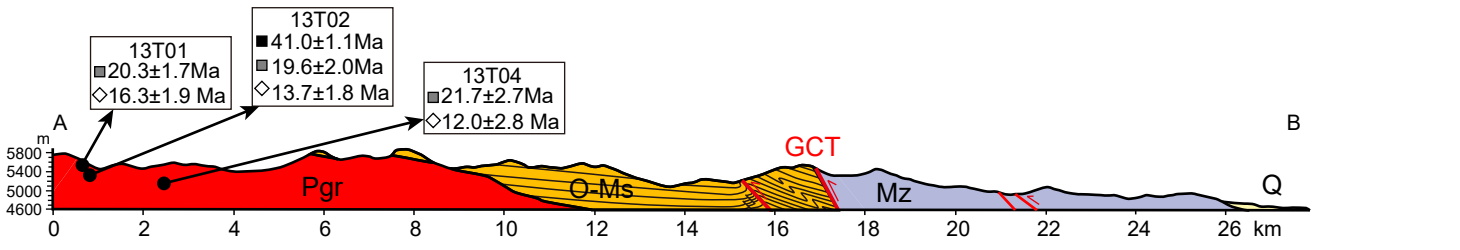

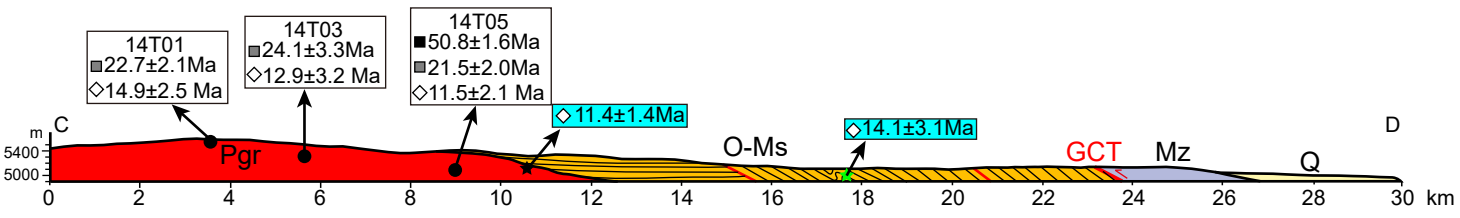

Figure 3.

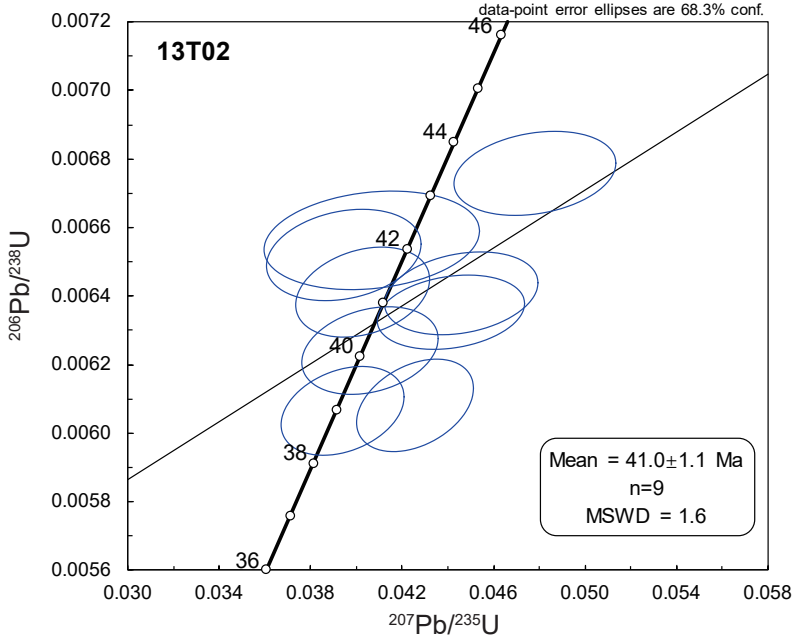
data-point error ellipses are 68.3% conf.
13T02
46
44
42
40
38
36
Mean = 41.0±1.1 Ma
n=9
MSWD = 1.6
0.0072
0.0070
0.0068
0.0066
0.0064
0.0062
0.0060
0.0058
0.0056
0.030
0.034
0.038
0.042
0.046
0.050
0.054
0.058
206Pb/238U
207Pb/235U

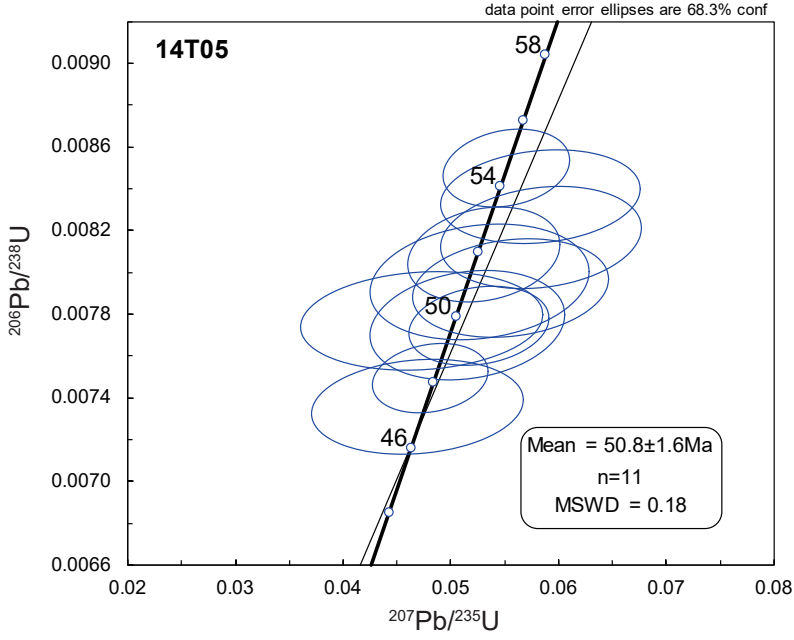
data point error ellipses are 68.3% conf
14T05
58
54
50
46
Mean = 50.8±1.6Ma
n=11
MSWD = 0.18
0.0090
0.0086
0.0082
0.0078
0.0074
0.0070
0.0066
0.02
0.03
0.04
0.05
0.06
0.07
0.08
206Pb/238U
207Pb/235U

Figure 4.

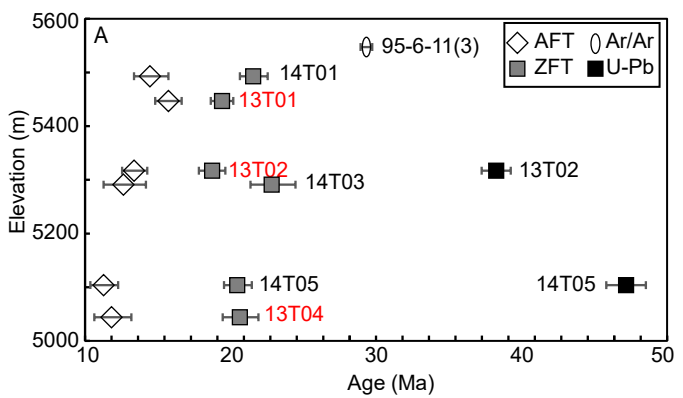
A
95-6-11(3)
AFT
Ar/Ar
ZFT
U-Pb
14T01
13T01
13T02
14T03
13T02
14T05
14T05
13T04
Elevation (m)
Age (Ma)

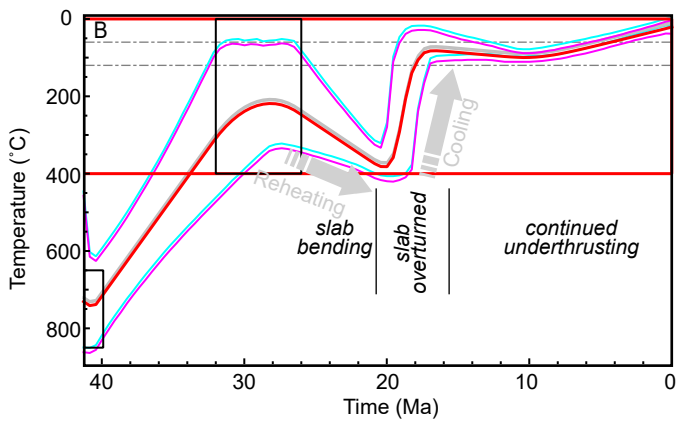
B
Cooling
Reheating
slab bending
slab overturned
continued underthrusting
Temperature (°C)
Time (Ma)

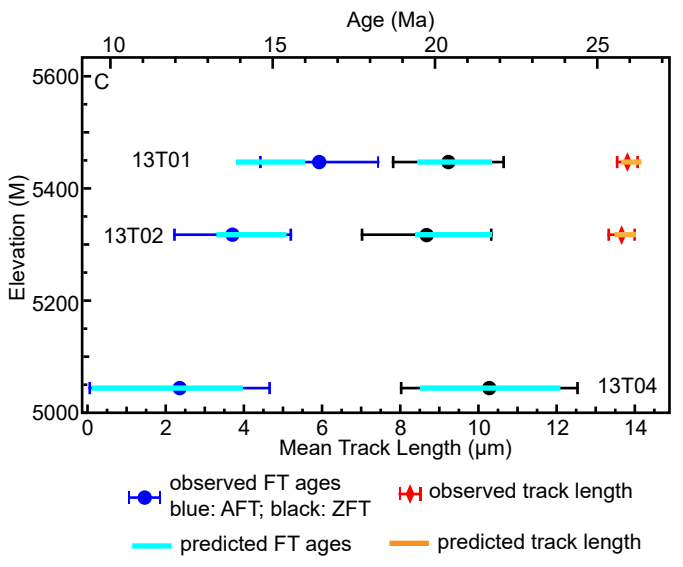
Age (Ma)
C
13T01
13T02
13T04
Elevation (M)
Mean Track Length (μm)
observed FT ages
blue: AFT; black: ZFT
observed track length
predicted FT ages
predicted track length

Figure 5.

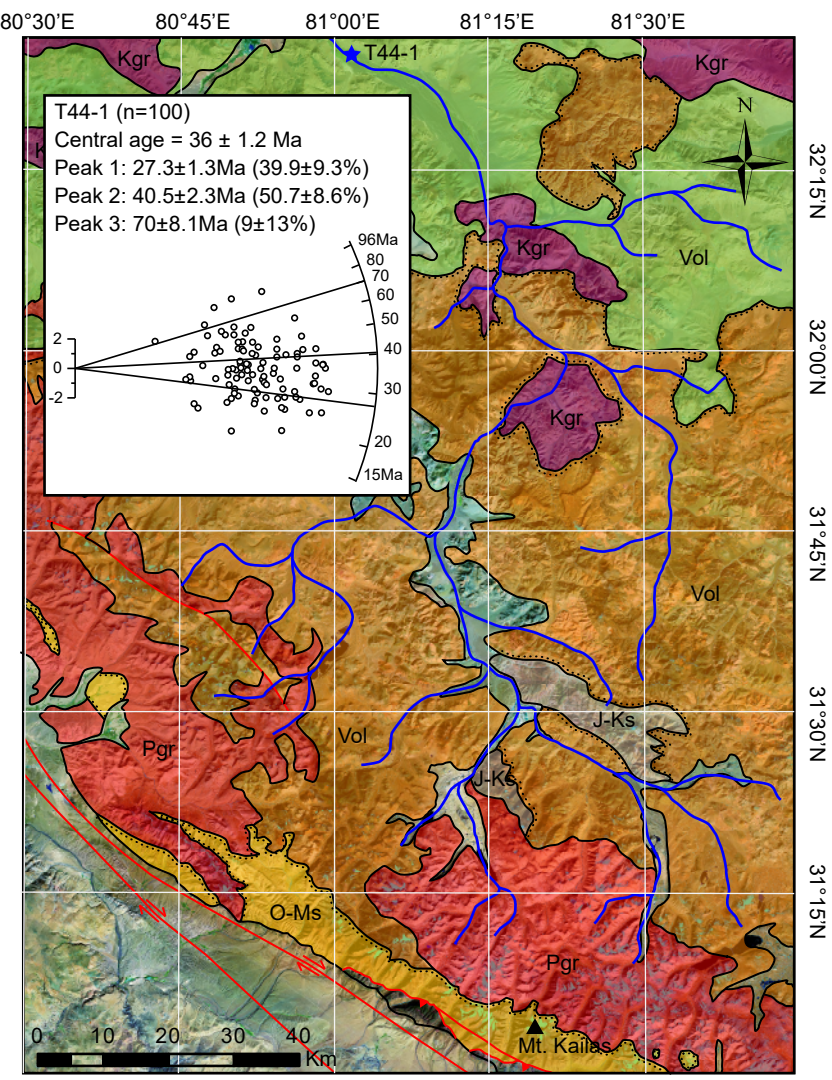

O-Ms	Kailas Formation	Vol	Cretaceous volcanics	Pgr	Gangdese batholith
Vol	Linzizong Group	J-Ks	J-K sedimentary rocks	Kgr	Cretaceous granite

Figure 6.

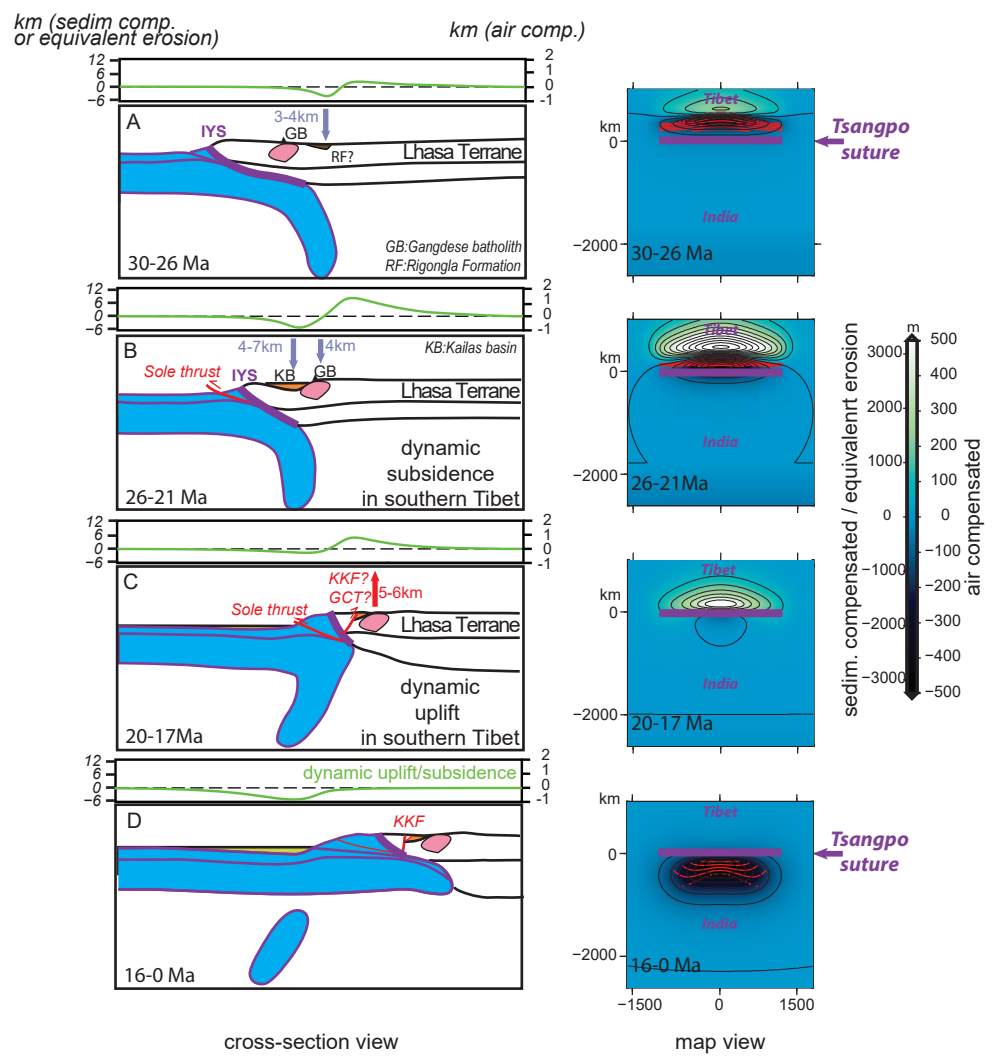
km (sedim comp.
or equivalent erosion)
km (air comp.)
12
6
0
−6
2
1
0
−1
A
IYS
3-4km
GB
RF?
Lhasa Terrane
GB:Gangdese batholith
RF:Rigongla Formation
30-26 Ma
B
4-7km
4km
KB:Kailas basin
Sole thrust
IYS
KB
GB
Lhasa Terrane
dynamic
subsidence
in southern Tibet
26-21 Ma
C
KKF?
GCT?
5-6km
Sole thrust
Lhasa Terrane
dynamic
uplift
in southern Tibet
20-17Ma
dynamic uplift/subsidence
D
KKF
16-0 Ma
cross-section view
km
0
−2000
Tibet
India
Tsangpo
suture
30-26 Ma
26-21Ma
20-17 Ma
16-0 Ma
−1500
0
1500
map view
m
3000
2000
1000
0
−1000
−2000
−3000
500
400
300
200
100
0
−100
−200
−300
−400
−500
sedim. compensated / equivalenrt erosion
air compensated

Figure 7.

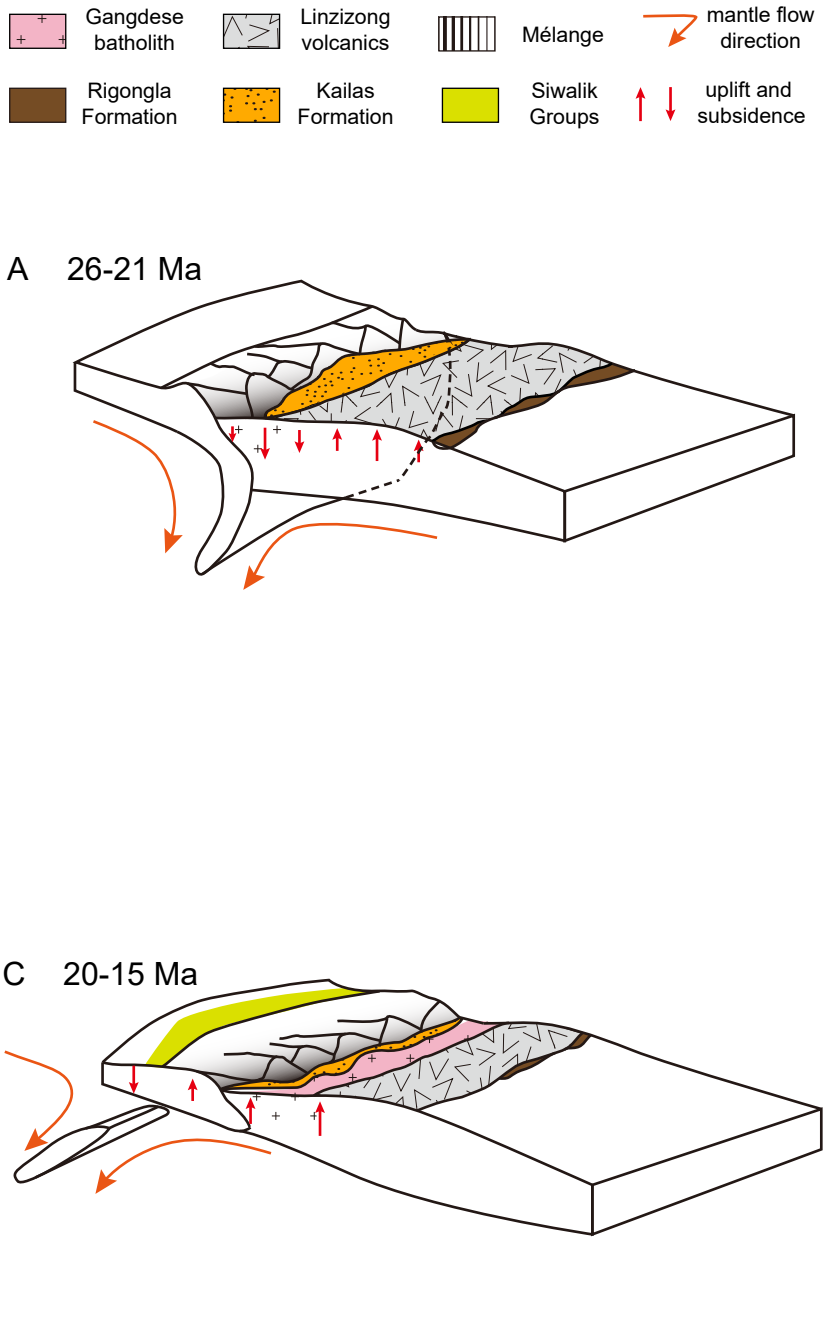
Gangdese batholith
Linzizong volcanics
Mélange
mantle flow direction
Rigongla Formation
Kailas Formation
Siwalik Groups
uplift and subsidence
A 26-21 Ma
B 26-21 Ma
deposition hindered by Himalayan topography
initial length of KB (endorheic condition)
deposition hindered by Gangdese relief
maximum theorical width
maximum theorical thickness
dynamic subsidence
evacuation of material along the river during the early - middle Miocene
N
Kailas basin
Gangdese batholith
mélange
Indian plate
KB remaining width
destroyed by tectonics
destroyed by erosion
eroded
KB remaining thickness
dynamic uplift
C 20-15 Ma
D 20-15 Ma
KKF
CCF
Kailas basin
Gangdese batholith
mélange
Indian plate

Figure 8.

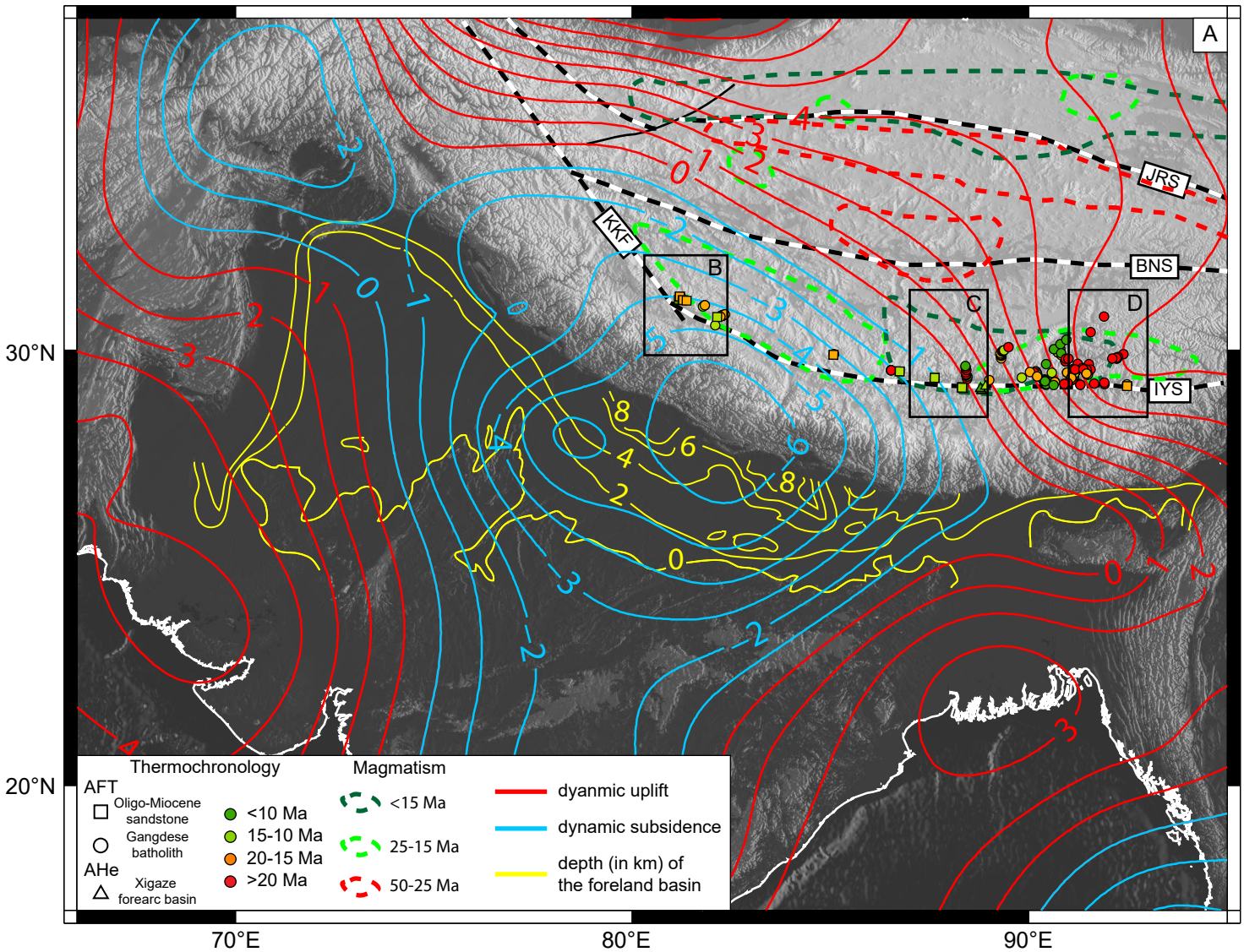
A
B
C
D
JRS
BNS
KKF
IYS
30°N
20°N
70°E
80°E
90°E
Thermochronology
AFT
Oligo-Miocene sandstone
Gangdese batholith
AHe
Xigaze forearc basin
<10 Ma
15-10 Ma
20-15 Ma
>20 Ma
Magmatism
<15 Ma
25-15 Ma
50-25 Ma
dyanmic uplift
dynamic subsidence
depth (in km) of the foreland basin

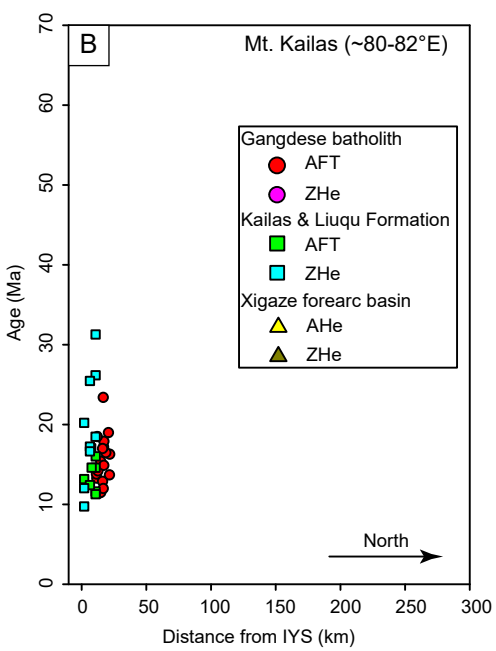
B
Mt. Kailas (~80-82°E)
Gangdese batholith
AFT
ZHe
Kailas & Liuqu Formation
AFT
ZHe
Xigaze forearc basin
AHe
ZHe
Age (Ma)
Distance from IYS (km)
North

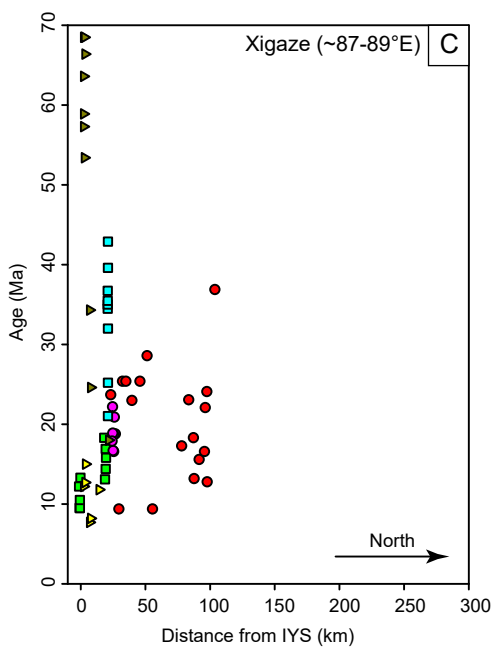
C
Xigaze (~87-89°E)
Age (Ma)
Distance from IYS (km)
North

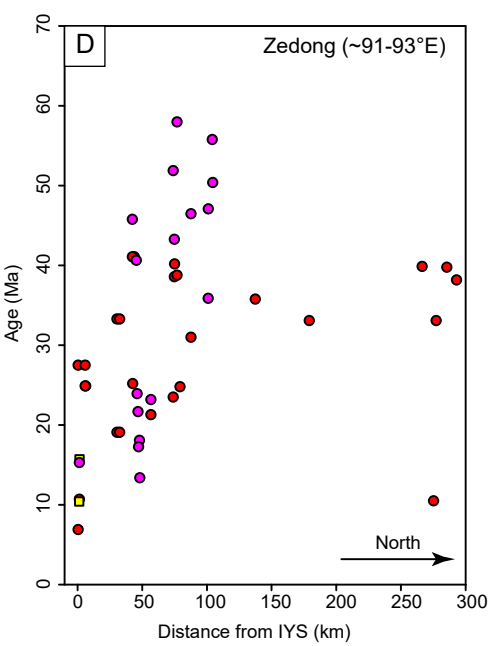
D
Zedong (~91-93°E)
Age (Ma)
Distance from IYS (km)
North